



# Influence of Thermal Treatment on the Thermal Conductivity of Beishan Granite

X. G. Zhao<sup>1</sup> · Z. Zhao<sup>2</sup> · Z. Guo<sup>1</sup> · M. Cai<sup>3,4</sup> · X. Li<sup>2</sup> · P. F. Li<sup>1</sup> · L. Chen<sup>1</sup> · J. Wang<sup>1</sup>

Received: 7 November 2017 / Accepted: 3 April 2018 / Published online: 12 April 2018  
© Springer-Verlag GmbH Austria, part of Springer Nature 2018

## Abstract

Granitic rocks are potential rock types for hosting high-level radioactive waste (HLW) repositories at depth. A better understanding of rock thermal conductivity is essential to develop HLW repositories successfully. In this work, experimental investigations on the thermal conductivity of thermally treated Beishan granite were conducted. Disk specimens preconditioned at 105 °C were heated to different temperatures (200, 300, 400, 550, 650, and 800 °C) and then cooled to room temperature for testing. Conventional physical properties such as bulk density, porosity, and P-wave velocity were measured under the effect of thermal treatment. Scanning electron microscope was used to characterize thermally induced microcracks in the rock. Thermal conductivities of the treated specimens under dry and water-saturated conditions were determined using the transient plane source method, and the effect of water saturation on the thermal conductivity was investigated. The influences of temperature and axial compression stress on the thermal conductivity were also studied. Results indicate that the thermal conductivity of the specimens depends strongly on the thermal treatment temperature. The thermal conductivity decreases nonlinearly with applied temperature, because of growth and propagation of microcracks in the specimens. On the other hand, water saturation plays an important role in increasing the thermal conductivity. In addition, significant differences exist in the thermal conductivity behaviors of the specimens when subjected to different ambient temperatures and compression stresses. Based on the experimental data, models considering the effect of porosity were established for describing the effects of water saturation, ambient temperature, and compression stress on the thermal conductivity of thermally treated rock.

**Keywords** Thermal conductivity · Thermal treatment · Microcracking · Water saturation · Ambient temperature · Compression stress · Beishan granite · Geological disposal

## List of symbols

$M_p$  Mass of rock preconditioned at 105 °C (g)  
 $M_t$  Mass of rock after thermal treatment (g)  
 $V_p$  Bulk volume of rock preconditioned at 105 °C (cm<sup>3</sup>)  
 $V_t$  Bulk volume of rock after thermal treatment (cm<sup>3</sup>)

$\rho_p$  Bulk density of rock preconditioned at 105 °C (g/cm<sup>3</sup>)  
 $\rho_t$  Bulk density of rock after thermal treatment (cm<sup>3</sup>)  
 $n_p$  Porosity of rock preconditioned at 105 °C (%)  
 $n_t$  Porosity of rock after thermal treatment (%)  
 $v_p$  P-wave velocity of rock preconditioned at 105 °C (m/s)  
 $v_t$  P-wave velocity of rock after thermal treatment (m/s)  
 $\lambda_{p\_dry}$  Thermal conductivity of rock preconditioned at 105 °C (W/mK)  
 $\lambda_{t\_dry}$  Thermal conductivity of rock after thermal treatment (W/mK)  
 $\lambda_{p\_sat}$  Thermal conductivity of untreated rock under water-saturated condition (W/mK)  
 $\lambda_{t\_sat}$  Thermal conductivity of thermally treated rock under water-saturated condition (W/mK)  
 $T_t$  Thermal treatment temperature (°C)  
 $T$  Ambient temperature (°C)

✉ X. G. Zhao  
xingguang100@126.com

- <sup>1</sup> CNNC Key Laboratory on Geological Disposal of High-level Radioactive Waste, Beijing Research Institute of Uranium Geology, Beijing 100029, China
- <sup>2</sup> Department of Civil Engineering, Tsinghua University, Beijing 100084, China
- <sup>3</sup> Bharti School of Engineering, Laurentian University, Sudbury, ON P3E 2C6, Canada
- <sup>4</sup> Key Laboratory of Ministry of Education for Safe Mining of Deep Metal Mines, Northeastern University, Shenyang 110004, China

$R_{mv}$	Mass variation ratio of rock before and after thermal treatment (%)
$R_{ve}$	Volume expansion ratio of rock before and after thermal treatment (%)
$S$	Effect of water saturation on rock thermal conductivity (%)
$S_t$	Effect of water saturation on thermal conductivity of thermally treated rock (%)
$\lambda_{t,T}$	Thermal conductivity of thermally treated rock at different ambient temperatures (W/mK)
$R_{t,r}$	Increase rate of thermal conductivity of thermally treated rock under uniaxial compression (%)
$\lambda_{t,l}$	Thermal conductivity of thermally treated rock at the last compression stress (W/mK)
$\lambda_{t,0}$	Thermal conductivity of thermally treated rock at zero stress (W/mK)
$R_t$	Thermal conductivity ratio of thermally treated rock under uniaxial compression
$\lambda_{t,c}$	Thermal conductivity of thermally treated rock subjected to different compression stresses (W/mK)
$\sigma_1$	Axial compression stress (MPa)
$\sigma_3$	Confining stress (MPa)
$A$	Fit coefficient
$B$	Fit coefficient
$C$	Fit coefficient

## 1 Introduction

Safe disposal of high-level radioactive waste (HLW) is a challenging rock engineering task for all countries using nuclear energy. HLW repositories can be situated in rocks that are suitable for permanent disposal of the HLW, such as granite, clay, rock salt, and tuff (Ahn and Apted 2010). Given that granitic rocks have low permeability, high thermal conductivity, and high strength, they have been considered as potential rock formations for hosting HLW repositories in some countries (Hudson et al. 2011). In China, site selection for a HLW repository started in 1985 (Wang 2010). So far, the Beishan area in Gansu Province of northwestern China, which contains many granite intrusions, has been recommended as the first priority area for the HLW repository (Wang 2014).

During the operation of a repository, the HLW will release heat continually and cause long-term temperature increases in the host rock. Thermal properties of the host rock determine rate of HLW heat dissipation. Among all the thermal properties of the host rock, the thermal conductivity is a key parameter to describe the heat transfer capability. For example, rocks with higher conductivities are more efficient at transferring heat energy. An accurate evaluation of host rock thermal conductivity is necessary for planning the

size, layout, and cost of HLW repository systems (Sundberg et al. 2009b). On the other hand, damage near the excavation boundary may occur as a result of sustained thermal loading, which may reduce the thermal conductivity of the host rock. Hence, a better understanding of the thermal conductivity of surrounding rocks under elevated temperatures is essential to designing HLW repositories.

Over the past few decades, considerable effort has been devoted to investigating the effect of high-temperature treatment on rock properties (Simmons and Cooper 1978; Heuze 1983; Homand-Etienne and Troalen 1984; Mahmutoglu 1998; David et al. 1999; Yavuz et al. 2010; Peng et al. 2016). It is widely accepted that for granitic rocks, thermally induced damage is dominantly driven by the growth of microcracks, which further leads to the deterioration of physical and mechanical properties of the rocks at the macroscopic scale. Experimental results indicate clearly how thermally induced microcracks modify porosity (Géraud 1994; Lima and Paraguassú 2004; Chaki et al. 2008; Zhang et al. 2016; Yang et al. 2017), elastic moduli (Heard and Page 1982; Yang et al. 2017), permeability (Michel et al. 1992; Chaki et al. 2008; Chen et al. 2017), acoustic velocities (Nasseri et al. 2007; Chaki et al. 2008; Inserra et al. 2013; Chen et al. 2017), and mechanical strength and deformation (Liu and Xu 2014; Shao et al. 2015; Sun et al. 2015; Chen et al. 2017; Yang et al. 2017; Kumari et al. 2018; Zhao et al. 2018) of granitic rocks. For example, Chaki et al. (2008) conducted tests on granite specimens subjected to various temperature treatments ranging from 105 to 600 °C and found that the porosity showed an increasing trend with increasing temperature, while the gas permeability and the longitudinal wave velocity decreased. Chen et al. (2017) investigated the evolution of permeability in Beishan granite heated from 100 to 800 °C and found that the permeability of the specimens changed approximately linearly with crack volumetric strain. Liu and Xu (2014) tested Qinling biotite granite specimens heated to a range of temperatures up to 1000 °C and confirmed that the uniaxial compressive strength and the tensile strength generally decreased with increasing temperature. Yang et al. (2017) carried out uniaxial compression tests to evaluate the effect of high-temperature treatment on crack damage, strength, and deformation failure characteristics of a granite. The results revealed that the crack damage stress, peak strength, and static elastic modulus of the specimens increased from 25 to 300 °C and then decreased up to the maximum tested temperature of 800 °C. In addition, they found that the mineral composition of granite did not change with increasing temperatures from 200 to 800 °C. Recently, Kumari et al. (2018) studied the mechanical and flow characteristics of Strathbogie granite after heating and water-cooling treatment (i.e., quenching). They found that when the specimens were quenched upon heating up to 600 °C, both strength and

elastic properties decreased significantly, and rock failure changed from brittle to quasi-brittle. However, with increasing confining pressures, permeability decreased nonlinearly. Increasing temperature also resulted in significant reductions in permeability (approximately 95% reduction from room temperature to 300 °C) as a result of thermally induced volumetric expansion, which leads to the enhancement of the interlock effect. While these studies provide meaningful insights into the physical and mechanical properties of thermally treated granite, experimental investigations into the influence of thermal treatment on the thermal conductivity are still limited.

From a microscopic perspective, thermal cracking in granite occurs via two different mechanisms (Richter and Simmons 1974; Chen and Wang 1980; Fredrich and Wong 1986; Wang et al. 1989; Jansen et al. 1993). First, mismatch and anisotropy in thermal expansion coefficients between adjacent crystalline grains in a homogeneous temperature field can result in sufficiently high stresses for the formation of thermal cycling cracks when the temperature exceeds a threshold. Second, thermal gradient cracks can also be generated when thermal stresses, due to an inhomogeneous temperature field, exceed the local tensile strength of the rock. To provide insight into the influence of heat treatment on rock properties, various methods have been employed to characterize thermally induced cracks in granitic rocks. For instance, based on scanning electron microscope (SEM) observations of granite specimens treated with temperatures ranging from 20 to 600 °C, Homand-Etienne and Houpert (1989) demonstrated that crack lengths barely changed, whereas crack widths increased with increasing temperature. Géraud (1994) conducted mercury injection tests coupled with SEM analysis to identify different porosity networks in granite specimens heated from 20 to 700 °C. Menéndez et al. (1999, 2001) used confocal scanning laser microscopy (CSLM) to characterize 3D crack networks in La Peyratte granite specimens in which microcracks were artificially induced by heating specimens at temperatures of 220 and 450 °C. According to optical thin sections and SEM images of Westerly granite after exposure to various temperature treatments ranging from 250 to 850 °C, Nasserri et al. (2007) found that both the total crack density and the crack width increased with increasing temperature. Freire-Lista et al. (2016) used polarizing petrographic and fluorescence microscopic techniques to investigate the development of thermal stress-induced microcracks in four granites subjected to thermal cycles from 20 to 105 °C. Using an X-ray micro-CT scanning system, Yang et al. (2017) analyzed the thermal damage characteristics of granite specimens and revealed that crack density within the specimens increased significantly with increasing temperature from 600 to 800 °C. Zhao

(2016) used a particle-based discrete element method to simulate thermally induced inter-grain or intra-grain microcracks in granite and showed that about 60% of the microcracks were of inter-granular microcracks. Based on these findings, it is concluded that the above-mentioned approaches are powerful for qualitative and quantitative evaluations of thermal cracking characteristics in granitic rocks. Although many studies have focused on characterizing thermally induced microcracks, only a few provide a comprehensive comparison of microstructure characteristics between untreated and thermally treated granite (Yang et al. 2017; Kumari et al. 2018).

It is well known that the thermal conductivity of rock is closely associated with mineral composition, porosity, texture, and density, etc. (Birch and Clark 1940; Clauser and Huenges 1995; Özkahraman et al. 2004; Hartmann et al. 2005; Ray et al. 2007; Sundberg et al. 2009a; Pasquale et al. 2015). For low-porosity granitic rocks, mineral composition is the dominant factor in thermal conductivity (Clauser and Huenges 1995). Water content, temperature, and compression stress also influence thermal conductivity of granitic rocks. Generally, thermal conductivity increases with increasing water content (Cho et al. 2009; Cho and Kwon 2010; Nagaraju and Roy 2014) and decreases with increasing temperature (Miao et al. 2014; Zhao et al. 2016). With increasing applied compression stress, the thermal conductivity starts to increase and subsequently the increase rate tends to be constant due to gradual closure of cracks and pores in the rock (Zhao et al. 2016). However, previous studies focused primarily on thermal conductivity behavior of naturally occurring granitic rocks; thermal conductivity characteristics of granite after thermal treatment have not been fully understood (Zhang et al. 2018). In particular, there is a distinct lack of information on the effects of various external factors such as water saturation, temperature, and compression stress on the thermal conductivity of rocks after high-temperature treatment. Moreover, the thermal conductivity of rocks in a potential HLW repository site must be characterized to provide necessary input conditions for safety assessment, which is one of the motivations for this work.

This paper aims at studying the thermal conductivity characteristics of Beishan granite after different temperature treatments using the transient plane source (TPS) method. In the following discussion, rock sampling and basic properties of the specimens are described first. Testing facilities and procedures are then introduced. Subsequently, the thermal conductivity and conventional physical parameters of the thermally treated specimens are measured, and the relationships between these parameters are discussed. The microstructure characteristics of the specimens before and after thermal treatment are also compared and analyzed using SEM images. The influences of water saturation,

temperature, and compression stress on the thermal conductivity of the thermally treated specimens are investigated comprehensively, and finally, some conclusions are obtained.

## 2 Specimen Preparation and Thermal Treatment

Rock sampling was conducted at the Xinchang site in the Beishan area. Intact drill cores were taken from borehole BS28, as shown in Fig. 1. The sampling depth was 35–40 m. The collected rock was fine- to medium-grained and was relatively isotropic in texture and composition (Fig. 2a). Three

thin sections were prepared and exposed to cross-polarized light to identify the dominant minerals. The analysis showed that the rock was comprised of approximately 54.7% plagioclase, 16.8% K-feldspar, 21.1% quartz, and 6.9% biotite and other accessory minerals such as zircon, apatite, and titanite. Figure 2b is a typical thin section photomicrograph showing the microstructure and mineralogical composition of the rock.

Altogether 42 rock specimens, 50 mm in diameter, were prepared from the drill cores, with a length to diameter ratio of approximately 0.5. To minimize thermal contact resistance during thermal conductivity measurements, specimen ends were polished carefully until the flatness and roughness

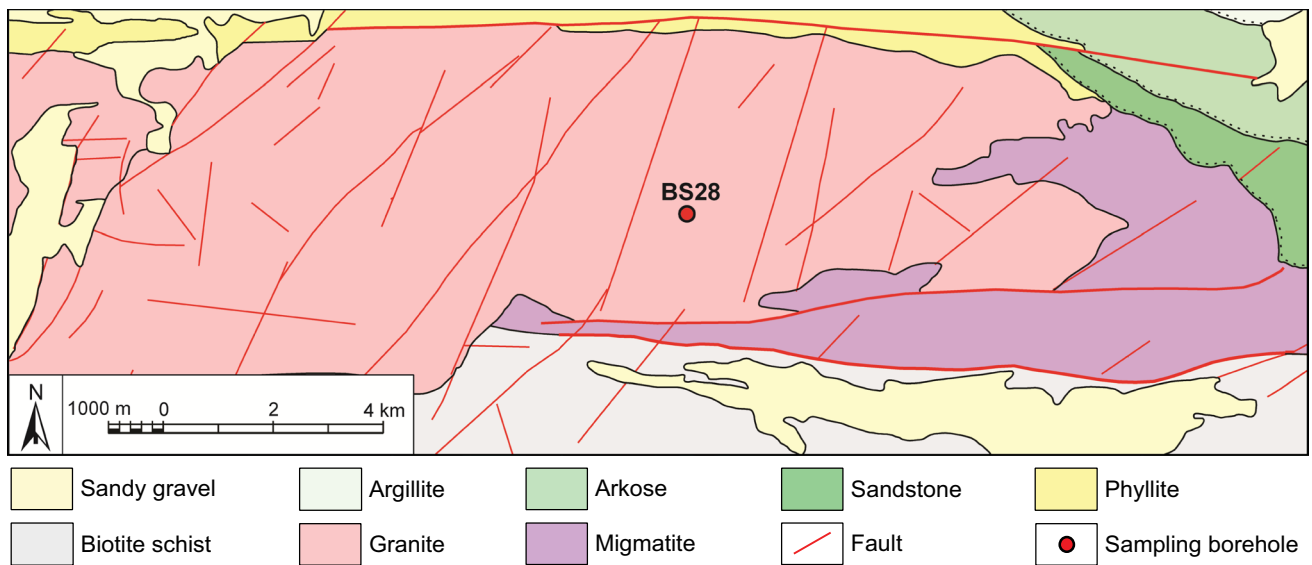


**Fig. 1** A simplified geological map of the Xinchang site in the Beishan area and sampling borehole location

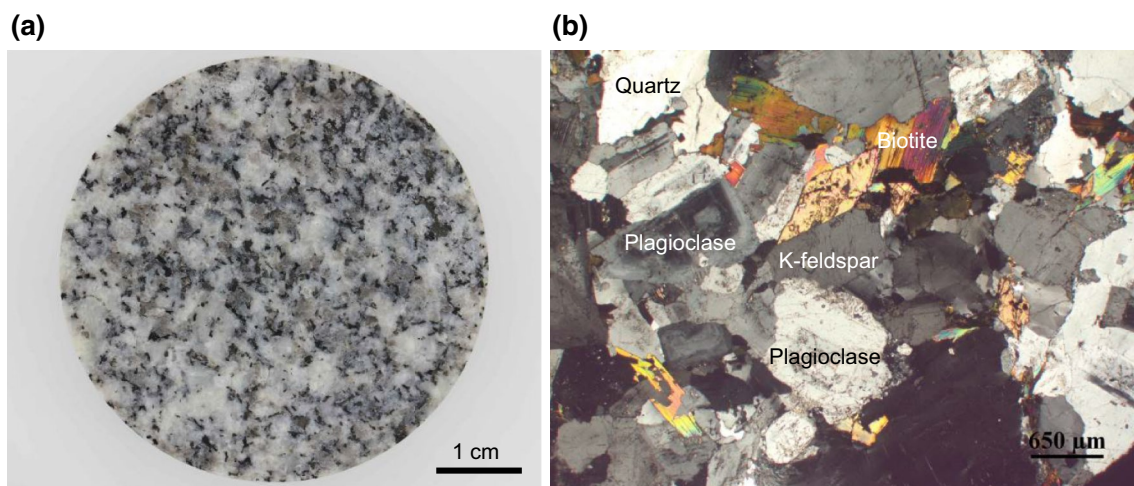


**Fig. 2** Observations of the fine- to medium-grained Beishan granite at different scales: **a** naked eye observation and **b** a thin section photomicrograph showing the main mineralogical composition of the rock

of the ends were  $< 10 \mu\text{m}$  and  $3 \mu\text{m}$ , respectively. Basic physical properties of the rock before thermal treatment were obtained in accordance with the specifications recommended by the International Society for Rock Mechanics (ISRM 1979). The specimens, which were preconditioned at  $105 \text{ }^\circ\text{C}$  for 24 h and then cooled to room temperature ( $21 \pm 1 \text{ }^\circ\text{C}$ ), had a bulk density of  $2.661 \text{ g/cm}^3$ , an average porosity of 0.65%, and an average P-wave velocity of  $4529 \text{ m/s}$ .

The preconditioned specimens were divided into seven groups, and each group contained three pairs of specimens. Before thermal treatment, thermal conductivities of all specimens were measured to provide a comparison between the undamaged and thermally damaged specimens. Six specimen groups were subjected to high-temperature treatments, i.e., at target temperatures of 200, 300, 400, 550, 650, and  $800 \text{ }^\circ\text{C}$ . The specimens were heated in a furnace at a rate of  $2 \text{ }^\circ\text{C/min}$  until the predefined target temperature was reached. The relatively low heating rate ensures a homogeneous temperature distribution within the specimens and avoids thermal shock during heating (Chaki et al. 2008; Yavuz et al. 2010). Subsequently, the target temperature was

held constant for 5 h, and then the specimens were cooled to room temperature naturally in the furnace. Finally, the thermally treated specimens were put into a desiccator for further testing.

### 3 Thermal Conductivity Measurement Methodology

The TPS method (Gustafsson 1991; Log and Gustafsson 1995) was employed to measure the thermal conductivity of the specimens. This method uses a transiently heated plane sensor (i.e., Hot Disk sensor) and a Hot Disk thermal constants analyzer (Fig. 3a). The adopted TPS2500S system can measure thermal conductivity of a material ranging from 0.01 to  $400 \text{ W/mK}$ . The Hot Disk sensor acts both as a heat source for increasing the temperature of the specimens and as a dynamic temperature sensor for recording the temperature increase. During the measurement, the temperature in the sensor rises and heat flows to the specimens. The temperature rise in the sensor provides an indicator of the

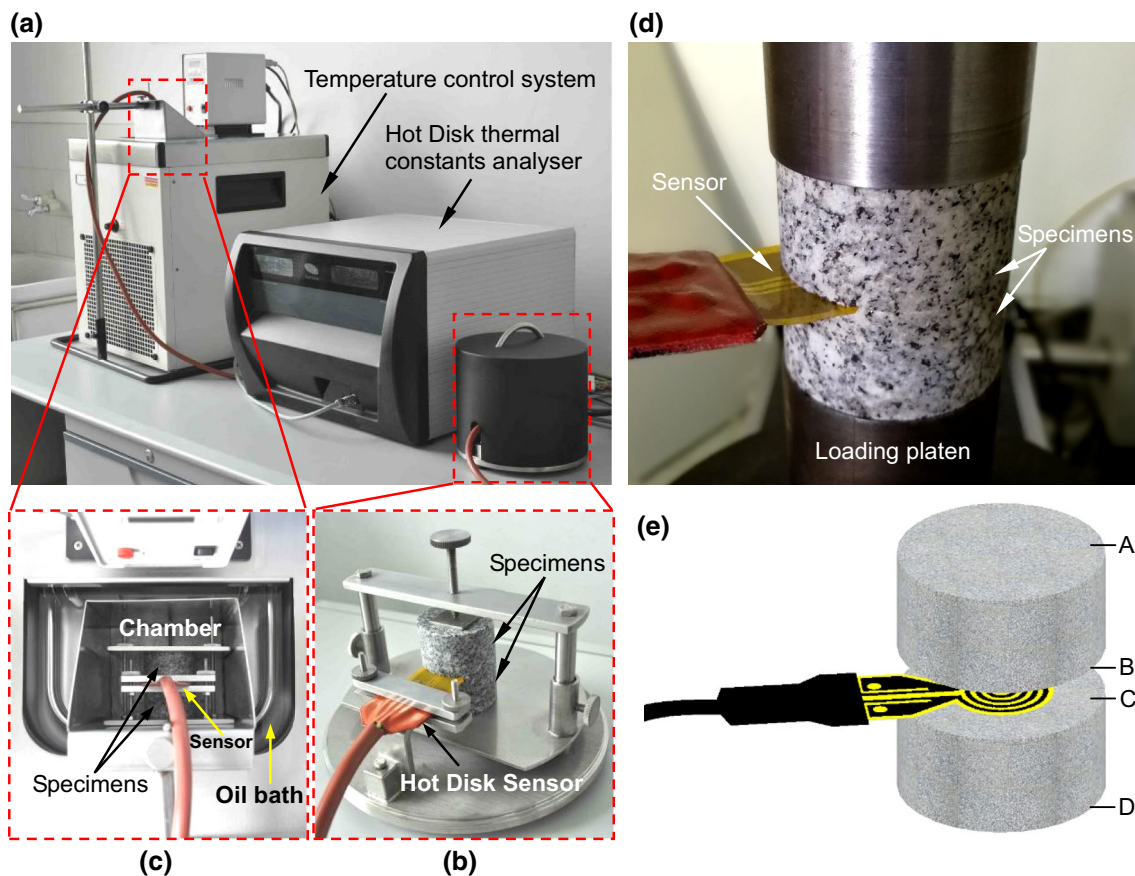


**Fig. 3** a The Hot Disk TPS2500S system. Thermal conductivity measurements of thermally treated specimens under different conditions: b room temperature, c high temperature, and d uniaxial com-

pression. e A schematic illustration of measuring thermal conductivity at four different interfaces (i.e., interfaces BC, AC, AD, and BD) between the specimen end surfaces

thermal properties of the specimens. If the specimens have good thermal conducting properties, heat will be transported rapidly into the specimens. Conversely, if the specimens have good thermal insulation properties, the sensor temperature will rise faster and heat will not be transported as efficiently. In this study, the Hot Disk sensor has a radius of 6.403 mm, which complies with the recommended relation between sensor radius and specimen geometry (Hot Disk 2007). The TPS method has been widely used to determine thermal properties of rock and other materials (Adl-Zarrabi 2004; Solórzano et al. 2008; Yang et al. 2012; Xu et al. 2014; Lagüela et al. 2015; Urquhart and Bauer 2015; Zhao et al. 2016). An introduction to the TPS technology and a brief comparison between several different thermal conductivity measurement methods can be found in (Gustafsson 1991; Zhao et al. 2016).

### 3.1 Tests on Thermally Treated Specimens Under Dry and Saturated Conditions

Thermal conductivity measurements were taken on dry specimens subjected to different temperature treatments. When performing measurements at room temperature ( $21 \pm 1$  °C), the Hot Disk sensor was placed horizontally between the two specimens (see Fig. 3b), and they were firmly clamped together to ensure that there was no air gap between the sensor and the specimen ends. After the test, specimens were immersed in deionized water in a vacuum for 96 h to saturate them (Zhao et al. 2016). Subsequently, the specimens were taken from the vacuum and the surfaces were wiped dry to measure the thermal conductivity under water-saturated conditions. The masses of the specimens before and after saturation were measured, and the porosity ( $n_p$ ) was calculated.

For each pair of thermally treated specimens, dried or saturated, four measurements of thermal conductivity were

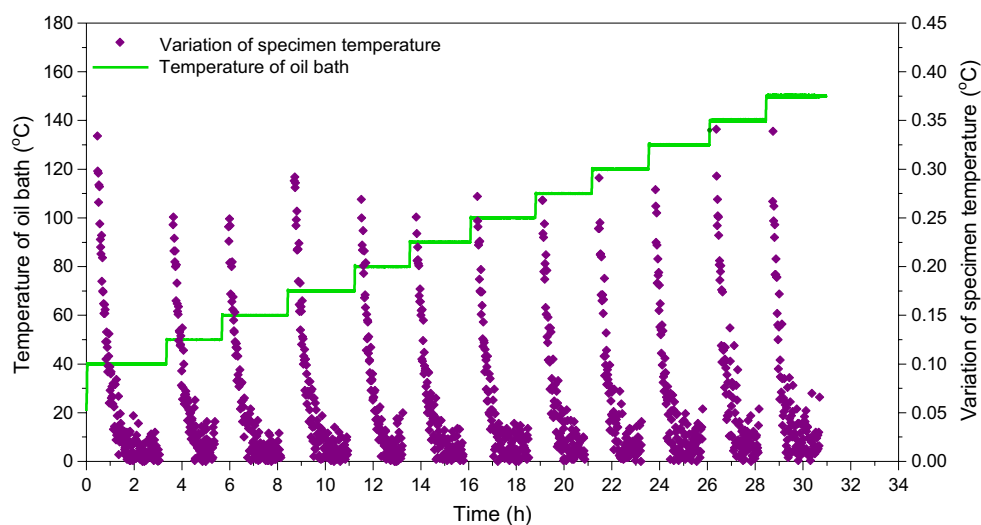
conducted at different interfaces (i.e., interfaces BC, AC, AD and BD) between the specimen end surfaces to reduce the influence of rock heterogeneity on the test results, as illustrated in Fig. 3e. Hence, the average thermal conductivity value obtained from the four measurements will be used in the following discussion. After water-saturated testing, the specimens were dehydrated in a thermostatic drying oven at 105 °C for 24 h (ISRM 1979) and then cooled in a desiccator for the temperature and compression stress-dependent thermal conductivity measurements.

### 3.2 Tests on Thermally Treated Specimens Under Increasing Temperature and Compression Stress

To study the effect of ambient temperature on thermal conductivity of the thermally damaged specimens, measurements were taken on seven pairs of specimens using a constant temperature oil bath and a temperature control system, as shown in Fig. 3c. The ambient temperature was varied from 40 to 150 °C. Thermal conductivity measurements were taken when the specimens in the chamber within the oil bath reached thermal equilibrium and maintained the target temperature values. During thermal equilibration of the oil bath, the Hot Disk sensor continually monitors temperature variations of the specimens, and a typical temperature–time history is presented in Fig. 4. Thermal conductivity was measured when the recorded temperature variation of the specimens was  $< 0.04$  °C (Zhao et al. 2016). It is seen from Fig. 4 that it took approximately 2.5 h for specimens to maintain a certain ambient temperature. Because experiments under various temperatures are so time-consuming, only one measurement was taken for each pair of specimens.

Thermal conductivity measurements were taken at room temperature ( $21 \pm 1$  °C) on thermally treated specimens under uniaxial compression using a hydraulic

**Fig. 4** Temperature–time relationships showing the variation of the oil bath temperature with time, and the evolution of specimen temperature variation during thermal conductivity measurements of a pair of thermally treated specimens



servo-controlled compression system. As presented in Fig. 3d, two specimens and the Hot Disk sensor were contained between steel loading platens. The interfaces between the specimens and the steel platens were daubed with a thin layer of lubricant to reduce end friction during loading. Axial load-controlled loading was used, with a loading rate of 100 N/s. The axial load was increased in increments of 5 MPa, and thermal conductivity was measured at each incremental stress level. The maximum compression stress applied was 45 MPa (Zhao et al. 2016).

## 4 Results

The basic physical parameters and thermal conductivities of the specimens before and after thermal treatment are listed in Table 1. For the seven specimen groups preconditioned at 105 °C, the average thermal conductivity ( $\lambda_{p,dry}$ ) ranges from 2.454 to 2.491 W/mK. Based on the average  $\lambda_{p,dry}$  of each rock group, a statistical analysis shows that the standard deviation (SD) and coefficient of variation (CoV) are <0.015 W/mK and 0.6%, respectively, indicating that results between specimen groups are very consistent. Meanwhile, the mean dry bulk density ( $\rho_p$ ), porosity ( $n_p$ ), and P-wave velocity ( $v_p$ ) also present good statistical regularities, with SD values of 0.003 g/cm<sup>3</sup>, 0.07%, and 48 m/s, respectively. The small dispersion of these initial physical parameters before thermal treatment demonstrates that specimens have good homogeneity; this is important for investigating the influence of thermal treatment on the thermal conductivity.

In the following discussion, averages of the measurements for all specimen groups are used to represent properties of the rock preconditioned at 105 °C. Analysis of the properties after thermal treatment uses averages of the measurements for the six specimen groups treated with high temperatures.

### 4.1 Effect of Thermal Treatment Temperature

According to the experimental results listed in Table 1, variation of thermal conductivity ( $\lambda_{t,dry}$ ) with thermal treatment temperature ( $T_t$ ) for thermally treated specimens is plotted in Fig. 5. A nonlinear, decreasing trend of  $\lambda_{t,dry}$  is seen with increasing  $T_t$ , and several typical stages can be observed. From 105 to 200 °C,  $\lambda_{t,dry}$  changes very little, which may indicate that thermally induced microcracking is not sufficient to influence the thermal conductivity. A gradual decrease in  $\lambda_{t,dry}$  occurs when  $T_t$  ranges between 200 and 400 °C, which may indicate that thermally induced microcracks are developing. When  $T_t$  increases up to 650 °C,  $\lambda_{t,dry}$  decreases rapidly and the decay rate of  $\lambda_{t,dry}$  peaks at temperatures ranging between 550 and 650 °C. This implies that microcracking has become more pronounced. The thermally induced microcracks act as barriers to heat flow and result in

considerable deterioration of the thermal conductivity. With further increase in  $T_t$  from 650 to 800 °C,  $\lambda_{t,dry}$  continues to decrease but at a decreasing decay rate, indicating that the high-temperature treatment further increases the number of microcracks, but at a slower rate. When  $T_t = 800$  °C, the magnitude of  $\lambda_{t,dry}$  is nearly half its value before thermal treatment, indicating a significant decrease in heat transfer capacity due to severe damage within the specimens.

To characterize thermally induced microcracks and interpret the decay of thermal conductivity with increasing thermal treatment temperature, SEM observations were performed on six small rectangular prism specimens of approximately 10×10×3 mm<sup>3</sup>. These small specimens were prepared from the rest of drill cores and were treated with different temperatures using the same procedure described above. After preconditioning at 105 °C but before thermal treatment, SEM images were obtained from the specimens to provide a comparison of microstructure characteristics between untreated and thermally treated specimens. During SEM imaging, the apparent minerals were identified by energy spectrum analysis.

Figure 6 shows SEM images of the specimens before and after thermal treatment. Compared with the result at  $T_t = 105$  °C, we can observe microstructural alterations in the specimen at  $T_t = 200$  °C (see Fig. 6a), i.e., the widths of pre-existing microcracks in the quartz grain decrease slightly. The thermally induced volumetric expansion of mineral grains at relatively low temperatures is possibly responsible for the closure of the microcracks in granitic rocks (Kumari et al. 2017, 2018; Yang et al. 2017). However, the slight microstructural alterations may have a negligible influence on the thermal conductivity. Hence,  $\lambda_{t,dry}$  is nearly constant for  $T_t = 105$  and 200 °C (see Fig. 5). When  $T_t$  is increased to 300 and 400 °C, inter-granular and intra-granular microcracks appear in the specimens. It is seen from Fig. 6b and c that inter-granular microcracks generate between biotite and quartz (points A, B, L, and O), quartz and plagioclase (points C and F), biotite and plagioclase (point G), biotite and K-feldspar (points H and I), and two biotite grain boundaries (points J and K). The widths of the observed inter-granular microcracks within the specimens treated at 300 and 400 °C are generally < 2 μm. Meanwhile, intra-granular microcracks occur along cleavage planes in biotite (points D and N). In addition, the width of pre-existing microcracks within quartz grains increases (points E and M). These microcracking behaviors are responsible for the observed gradual reduction of  $\lambda_{t,dry}$  for temperatures between 200 and 400 °C.

The treatment temperature of 400 °C is a temperature threshold, triggering rapid changes in thermally induced crack widths. Inter-granular and intra-granular microcrack widths increase significantly as  $T_t$  increases to 550 °C. As shown in Fig. 6d, the observed microcracks between biotite

**Table 1** Basic physical parameters and thermal conductivities of the specimens before and after thermal treatment

Group no.	Specimen pair no.	Properties of the specimens preconditioned at 105 °C					$T_1$ (°C)	Properties of the specimens after thermal treatment								
		$M_p$ (g)	$V_p$ (cm <sup>3</sup> )	$\rho_p$ (g/cm <sup>3</sup> )	$n_p$ (%)	$v_p$ (m/s)		$\lambda_{p,dry}$ (W/mK)	$\lambda_{p,sat}$ (W/mK)	$M_t$ (g)	$V_t$ (cm <sup>3</sup> )	$\rho_t$ (g/cm <sup>3</sup> )	$n_t$ (%)	$v_t$ (m/s)	$\lambda_{t,dry}$ (W/mK)	$\lambda_{t,sat}$ (W/mK)
1	BS28-1-1	131.053	49.189	2.664	0.65	4499	2.476	2.695	-	-	-	-	-	-	-	
	BS28-1-2	127.067	47.709	2.663	0.65	4523	2.481	2.758	-	-	-	-	-	-	-	
	BS28-1-3	126.768	47.620	2.662	0.66	4642	2.432	2.716	-	-	-	-	-	-	-	
	<b>Mean</b>	<b>128.296</b>	<b>48.173</b>	<b>2.663</b>	<b>0.65</b>	<b>4555</b>	<b>2.463</b>	<b>2.723</b>	-	-	-	-	-	-	-	
	<b>SD</b>	-	-	<b>0.001</b>	<b>0.01</b>	<b>77</b>	<b>0.027</b>	<b>0.032</b>	-	-	-	-	-	-	-	
2	BS28-2-1	131.607	49.560	2.656	0.71	4510	2.377	2.705	200	131.592	49.593	2.653	0.65	4281	2.381	2.563
	BS28-2-2	131.450	49.448	2.658	0.69	4566	2.516	2.828	-	131.427	49.428	2.659	0.67	4160	2.503	2.729
	BS28-2-3	131.478	49.353	2.664	0.71	4626	2.564	2.759	-	131.455	49.359	2.663	0.65	4322	2.543	2.760
	<b>Mean</b>	<b>131.512</b>	<b>49.454</b>	<b>2.659</b>	<b>0.70</b>	<b>4567</b>	<b>2.486</b>	<b>2.764</b>	-	<b>131.491</b>	<b>49.460</b>	<b>2.659</b>	<b>0.66</b>	<b>4254</b>	<b>2.476</b>	<b>2.684</b>
	<b>SD</b>	-	-	<b>0.004</b>	<b>0.01</b>	<b>58</b>	<b>0.097</b>	<b>0.062</b>	-	-	-	<b>0.005</b>	<b>0.01</b>	<b>84</b>	<b>0.084</b>	<b>0.106</b>
3	BS28-3-1	131.912	49.606	2.659	0.71	4519	2.400	2.683	300	131.867	49.623	2.657	0.78	3435	2.238	2.572
	BS28-3-2	131.916	49.652	2.657	0.73	4440	2.520	2.832	-	131.872	49.695	2.654	0.77	3517	2.351	2.688
	BS06-3-3	131.542	49.481	2.658	0.69	4508	2.520	2.801	-	131.497	49.527	2.655	0.72	3619	2.367	2.679
	<b>Mean</b>	<b>131.790</b>	<b>49.580</b>	<b>2.658</b>	<b>0.71</b>	<b>4489</b>	<b>2.480</b>	<b>2.772</b>	-	<b>131.745</b>	<b>49.615</b>	<b>2.655</b>	<b>0.76</b>	<b>3524</b>	<b>2.319</b>	<b>2.646</b>
	<b>SD</b>	-	-	<b>0.001</b>	<b>0.02</b>	<b>43</b>	<b>0.069</b>	<b>0.079</b>	-	-	-	<b>0.002</b>	<b>0.03</b>	<b>92</b>	<b>0.070</b>	<b>0.065</b>
4	BS28-4-1	132.129	49.728	2.657	0.72	4536	2.397	2.709	400	132.064	49.841	2.650	0.90	3118	2.158	2.504
	BS28-4-2	131.679	49.577	2.656	0.70	4476	2.513	2.808	-	131.610	49.702	2.648	0.90	3114	2.223	2.606
	BS28-4-3	132.018	49.669	2.658	0.68	4728	2.562	2.828	-	131.944	49.755	2.652	0.86	3116	2.275	2.634
	<b>Mean</b>	<b>131.942</b>	<b>49.658</b>	<b>2.657</b>	<b>0.70</b>	<b>4580</b>	<b>2.491</b>	<b>2.782</b>	-	<b>131.873</b>	<b>49.766</b>	<b>2.650</b>	<b>0.89</b>	<b>3116</b>	<b>2.219</b>	<b>2.581</b>
	<b>SD</b>	-	-	<b>0.001</b>	<b>0.02</b>	<b>132</b>	<b>0.085</b>	<b>0.064</b>	-	-	-	<b>0.002</b>	<b>0.02</b>	<b>2</b>	<b>0.059</b>	<b>0.068</b>
5	BS28-5-1	131.551	49.508	2.657	0.70	4506	2.454	2.723	550	131.384	49.907	2.633	1.52	2088	1.858	2.419
	BS28-5-2	131.277	49.369	2.659	0.69	4607	2.514	2.779	-	131.109	49.708	2.638	1.52	2126	1.885	2.478
	BS28-5-3	131.409	49.297	2.666	0.68	4588	2.499	2.716	-	131.247	49.741	2.639	1.54	2047	1.841	2.483
	<b>Mean</b>	<b>131.412</b>	<b>49.391</b>	<b>2.661</b>	<b>0.69</b>	<b>4567</b>	<b>2.489</b>	<b>2.739</b>	-	<b>131.247</b>	<b>49.785</b>	<b>2.637</b>	<b>1.53</b>	<b>2087</b>	<b>1.861</b>	<b>2.460</b>
	<b>SD</b>	-	-	<b>0.005</b>	<b>0.01</b>	<b>54</b>	<b>0.031</b>	<b>0.035</b>	-	-	-	<b>0.003</b>	<b>0.01</b>	<b>40</b>	<b>0.022</b>	<b>0.036</b>
6	BS28-6-1	131.303	49.281	2.664	0.56	4516	2.448	2.660	650	131.069	50.598	2.590	3.35	1156	1.408	2.405
	BS28-6-2	131.139	49.235	2.664	0.56	4410	2.404	2.638	-	130.905	50.545	2.590	3.37	1174	1.402	2.368
	BS28-6-3	131.075	49.218	2.663	0.57	4493	2.511	2.745	-	130.851	50.491	2.592	3.33	1168	1.428	2.513
	<b>Mean</b>	<b>131.172</b>	<b>49.245</b>	<b>2.664</b>	<b>0.56</b>	<b>4473</b>	<b>2.454</b>	<b>2.681</b>	-	<b>130.942</b>	<b>50.545</b>	<b>2.591</b>	<b>3.35</b>	<b>1166</b>	<b>1.413</b>	<b>2.429</b>
	<b>SD</b>	-	-	<b>0.001</b>	<b>0.01</b>	<b>56</b>	<b>0.054</b>	<b>0.057</b>	-	-	-	<b>0.001</b>	<b>0.02</b>	<b>9</b>	<b>0.014</b>	<b>0.075</b>
7	BS28-7-1	131.434	49.382	2.662	0.56	4464	2.557	2.904	800	131.124	50.929	2.575	3.99	975	1.350	2.502
	BS28-7-2	130.862	49.133	2.663	0.56	4485	2.430	2.694	-	130.539	50.718	2.574	4.14	933	1.277	2.353
	BS28-7-3	131.097	49.241	2.662	0.56	4469	2.447	2.684	-	130.777	50.822	2.573	4.23	936	1.286	2.381
	<b>Mean</b>	<b>131.131</b>	<b>49.252</b>	<b>2.662</b>	<b>0.56</b>	<b>4473</b>	<b>2.478</b>	<b>2.761</b>	-	<b>130.813</b>	<b>50.823</b>	<b>2.574</b>	<b>4.12</b>	<b>948</b>	<b>1.304</b>	<b>2.412</b>



Table 1 (continued)

Group no.	Specimen pair no.	Properties of the specimens preconditioned at 105 °C					$T_t$ (°C)	Properties of the specimens after thermal treatment							
		$M_p$ (g)	$V_p$ (cm <sup>3</sup> )	$\rho_p$ (g/cm <sup>3</sup> )	$n_p$ (%)	$v_p$ (m/s)		$\lambda_{p,dry}$ (W/mK)	$\lambda_{p,sat}$ (W/mK)	$M_t$ (g)	$V_t$ (cm <sup>3</sup> )	$\rho_t$ (g/cm <sup>3</sup> )	$n_t$ (%)	$v_t$ (m/s)	$\lambda_{t,dry}$ (W/mK)
SD	-	-	-	<b>0.001</b>	<b>0</b>	<b>11</b>	<b>0.069</b>	<b>0.124</b>	-	-	<b>0.001</b>	<b>0.12</b>	<b>23</b>	<b>0.040</b>	<b>0.079</b>
SD for all groups	-	-	<b>0.003</b>	<b>0.07</b>	<b>48</b>	<b>0.014</b>	<b>0.035</b>	-	-	-	-	-	-	-	-

The mean and standard deviation (SD) values of physical parameters for different groups are indicated by bold font

$M$ : mass;  $V$ : bulk volume;  $\rho$ : bulk density;  $n$ : porosity;  $v$ : P-wave velocity;  $\lambda_{p,dry}$ : thermal conductivity of the specimen preconditioned at 105 °C;  $\lambda_{p,sat}$ : thermal conductivity of the untreated specimen under water-saturated condition;  $T_t$ : thermal treatment temperature;  $\lambda_{t,dry}$ : thermal conductivity of the specimen after thermal treatment;  $\lambda_{t,sat}$ : thermal conductivity of the thermally treated specimen under water-saturated condition. Subscripts “p” and “t” indicate the values of the specimens preconditioned at 105 °C and after thermal treatment, respectively. Note that for each specimen pair,  $\lambda_{p,dry}$  is the average value calculated from four measurements at different interfaces between the specimen end surfaces, while  $\lambda_{p,sat}$  is obtained from one or two measure-

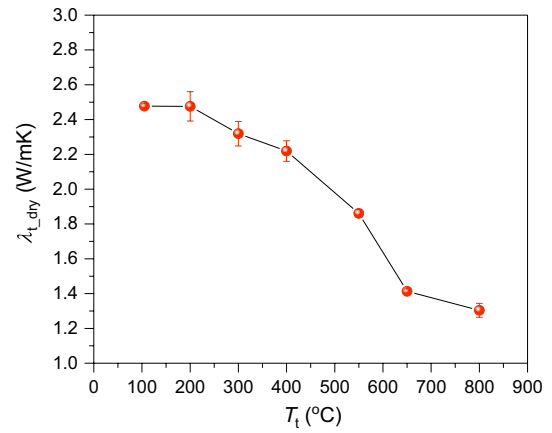
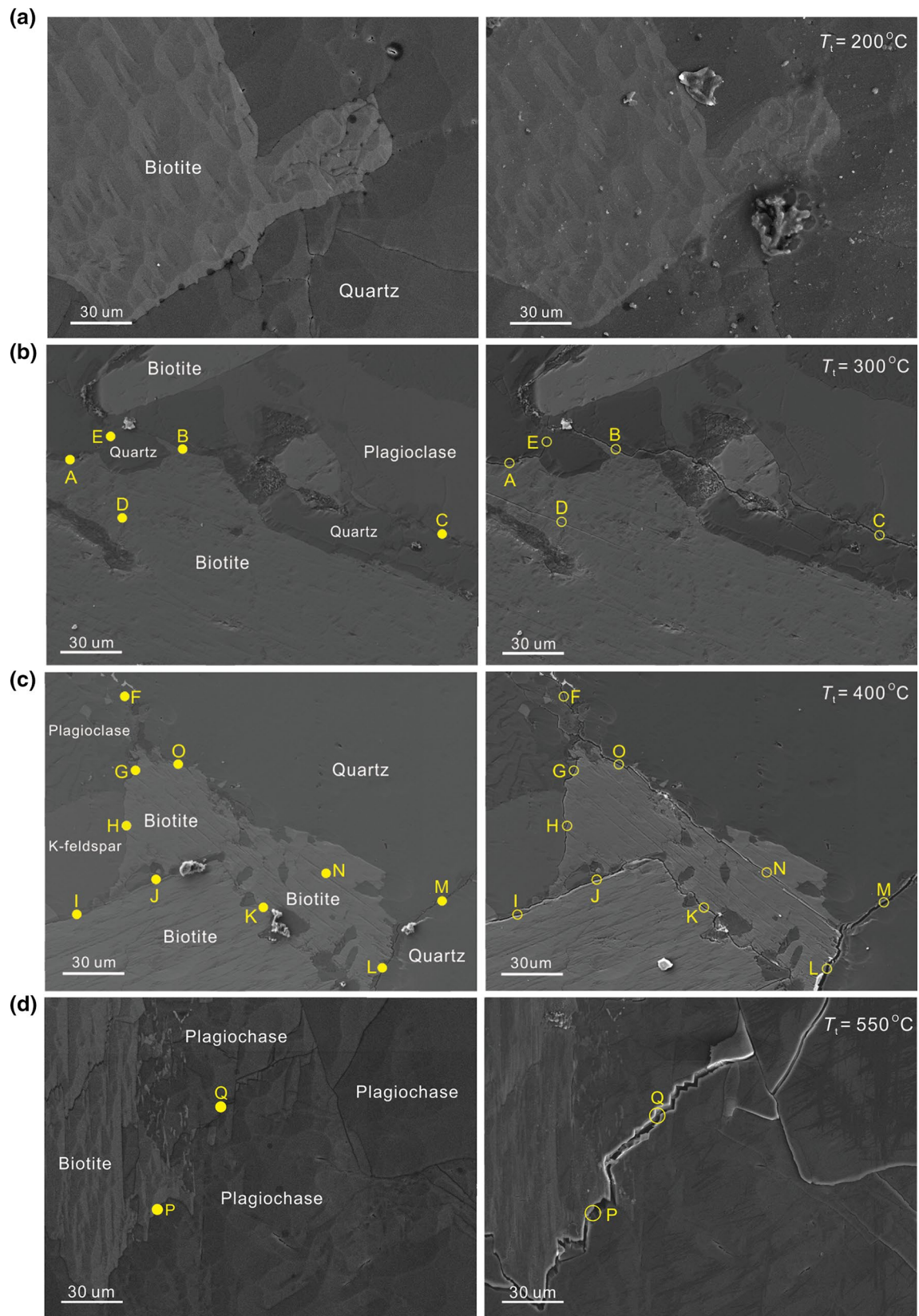


Fig. 5 Influence of thermal treatment temperature on thermal conductivity of Beishan granite. Error bars indicate the standard deviation of thermal conductivity

and plagioclase grain boundaries (point P) and along the cleavage plane of a plagioclase grain (point Q) have a maximum width of approximately 4  $\mu\text{m}$ . When  $T_t$  is further increased to 650 °C, increases in crack density and crack width become more pronounced. For example, it can be observed from Fig. 6e that many microcracks are generated in biotite grains, approximately parallel to cleavage planes (points R and S). The maximum widths of inter-granular microcracks between biotite and quartz grains, and of intra-granular microcracks within quartz grains, are about 8  $\mu\text{m}$  (points T and U). Hence, the decreasing rate of  $\lambda_{t,dry}$  becomes remarkable for treatment temperatures between 550 and 650 °C (see Fig. 5). When  $T_t$  is equal to 800 °C, inter-granular, intra-granular, and trans-granular microcracks distribute on the specimen surface, as shown in Fig. 6f. In addition to microcracks between plagioclase and K-feldspar grain boundaries (points V and X), some microcracks exist within the mineral grains. Also, a trans-granular microcrack with a maximum width of approximately 10  $\mu\text{m}$  passes through the plagioclase and K-feldspar grains (points W and Y). The intersection and coalescence of these different types of microcracks indicate that the treatment temperature of 800 °C has caused severe damage to the rock, leading to a significant decay of its capacity to transfer heat. Hence, the decrease in thermal conductivity of the specimens subjected to thermal treatment can be qualitatively explained by microcracking.

Different states of water (i.e., attached water, bound water, and mineral combined water) exist inside natural rocks. As analyzed by Zhang et al. (2016), attached water will escape between 70 and 100 °C. Bound water can only escape when the temperature is higher than 100 °C. Specifically, weakly bound water can escape at a temperature of approximately 150 °C, while strongly bound water can only escape at temperatures ranging between 200 and 300 °C. When the



**Fig. 6** SEM observations of thermally induced microcracks in Beishan granite treated with different temperatures: **a** 200 °C, **b** 300 °C, **c** 400 °C, **d** 550 °C, **e** 650 °C, and **f** 800 °C. (Left column, before thermal treatment; right column, after thermal treatment)

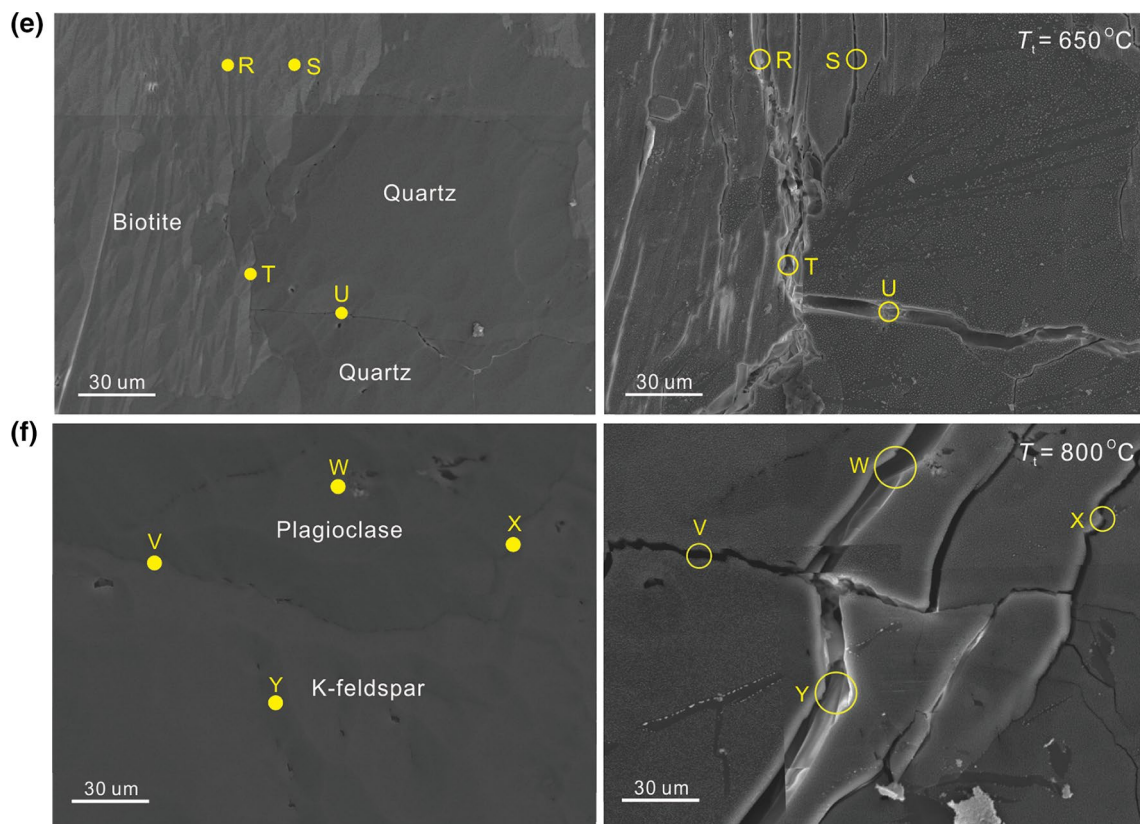


Fig. 6 (continued)

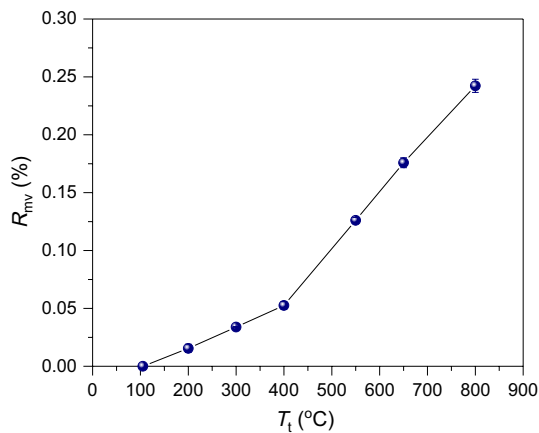
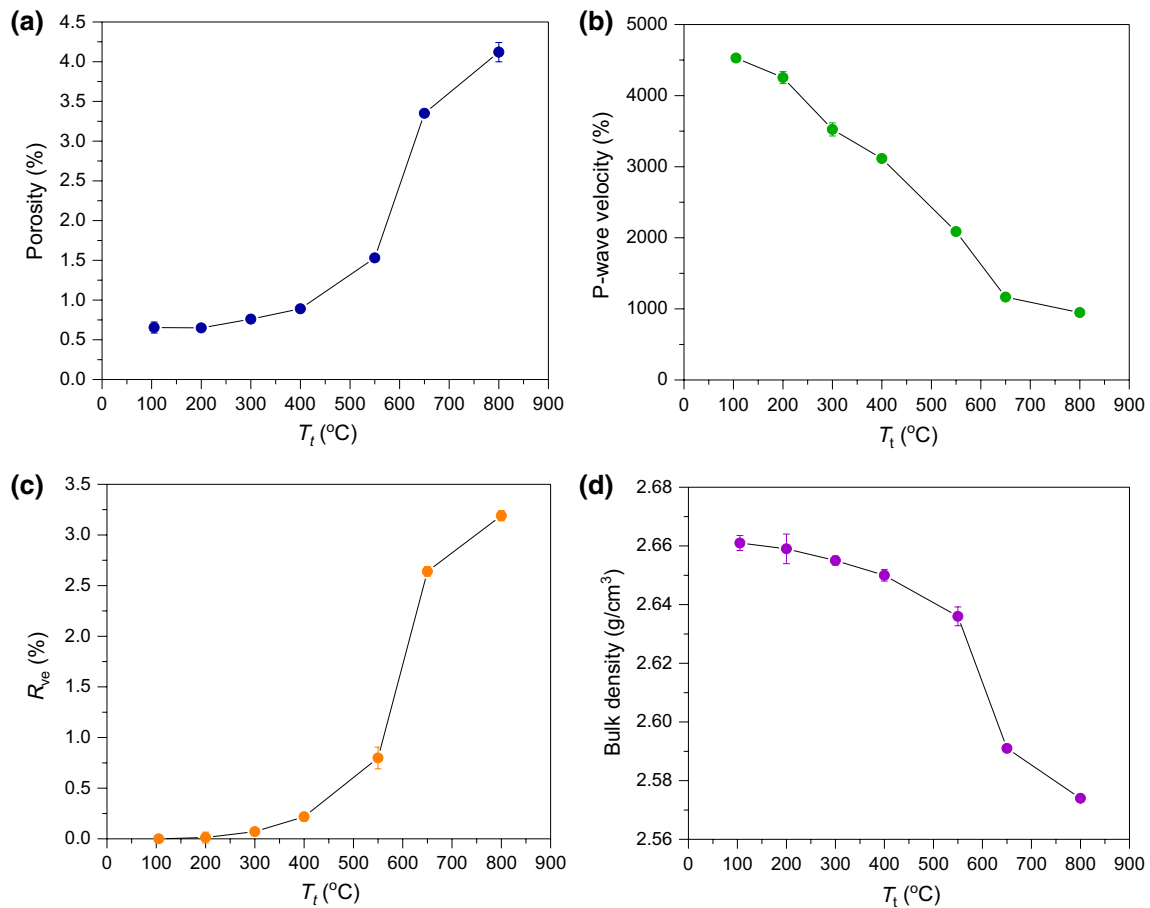


Fig. 7 Influence of thermal treatment temperature on the mass variation ratio ( $R_{mv} = (M_p - M_i)/M_p$ )

temperature exceeds 400 °C, mineral combined water may evaporate, which can lead to damage of mineral crystalline structures. To quantify the loss of water within specimens when subjected to different high-temperature treatments, the masses of the specimens preconditioned at 105 °C and after thermal treatment were measured (see Table 1). The mass variation ratio ( $R_{mv}$ ) was calculated, and results are shown in

Fig. 7. With increasing  $T_t$  from 105 to 400 °C,  $R_{mv}$  increases nearly linearly. When  $T_t$  ranges between 400 and 800 °C,  $R_{mv}$  increases approximately linearly, at a higher rate. This means that at the thermal treatment temperature threshold of 400 °C, water within the specimens starts to escape rapidly. The loss of different forms of water during thermal treatment may be another factor in the decrease in thermal conductivity of the specimens. However, compared with air within the thermally induced microcracks, the role of water loss in decreasing the thermal conductivity is minor because at a temperature of approximately 27 °C, the air has a lower thermal conductivity [0.026 W/mK (Hilsenrath et al. 1955)] than water [0.610 W/mK (Ramires et al. 1995)].

As suggested by some researchers (Chaki et al. 2008; Chen et al. 2017), porosity and P-wave velocity are two effective indicators to characterize thermally induced damage in granite. As shown in Fig. 8a, a slight increase in porosity from 0.65 to 0.89% occurs when  $T_t$  ranges between 105 and 400 °C. This may mean that the thermally treated specimens experience only minor structural modifications for this range of temperatures (Chaki et al. 2008). A rapid increase in porosity from 0.89 to 3.35% appears between 400 and 650 °C, indicating a significant increase in thermally induced microcracks, which leads to a remarkable decrease in thermal conductivity (see Fig. 5).



**Fig. 8** Variations of conventional physical properties of the thermally treated specimens with thermal treatment temperature: **a** porosity, **b** P-wave velocity, **c** volumetric expansion ratio ( $R_{ve} = (V_t - V_p)/V_p$ ), and **d** bulk density

When  $T_t$  ranges between 650 and 800 °C, the rate of porosity increase starts to slow, resulting in a decrease in the thermal conductivity decay rate. The variation of porosity within specimens affects ultrasonic wave propagation through the specimens. Similar to the  $\lambda_{t,dry} - T_t$  relationship (see Fig. 5), the P-wave velocity of thermally treated specimens decreases with increasing  $T_t$  due to gradual damage, and the maximum decay rate takes place when  $T_t$  ranges between 550 and 650 °C, as shown in Fig. 8b. The growth of thermally induced microcracks leads to increasing specimen volume at the macroscopic scale. The volume expansion ratio ( $R_{ve}$ ) of treated specimens increases nonlinearly with increasing  $T_t$  (Fig. 8c), similar to the response of porosity (see Fig. 8a). The volumetric expansion of the specimens causes a decrease in bulk density, which behaves as the inverse of porosity (see Fig. 8d). Hence, variations of porosity, P-wave velocity, volume expansion ratio, and bulk density reveal thermally induced damage characteristics of the specimens from a macroscopic point of view and also reflect changes in thermal conductivity with treatment temperature.

Based on the above analysis, it is clear that the thermal conductivity depends strongly on thermal treatment temperature. In addition, the thermal conductivity is closely related to other physical parameters. For example, Fig. 9 shows the variations of  $\lambda_{t,dry}$  with porosity, P-wave velocity, and bulk density of the specimens after thermal treatment. P-wave velocity and bulk density are directly proportional to thermal conductivity, while porosity is inversely proportional. These relationships can be described using positive or negative power functions (shown in Fig. 9).

## 4.2 Effect of Water Saturation

Figure 10 shows variations of average thermal conductivity values for the same set of thermally treated specimens under water-saturated conditions ( $\lambda_{t,sat}$ ) with  $T_t$ . It is seen that although  $\lambda_{t,sat}$  decreases with increasing  $T_t$ , values only range from 2.412 to 2.746 W/mK. Especially when  $T_t$  exceeds 550 °C,  $\lambda_{t,sat}$  decays slightly. This behavior is significantly different from that of thermally treated specimens under dry conditions, in which a notable decay of  $\lambda_{t,dry}$

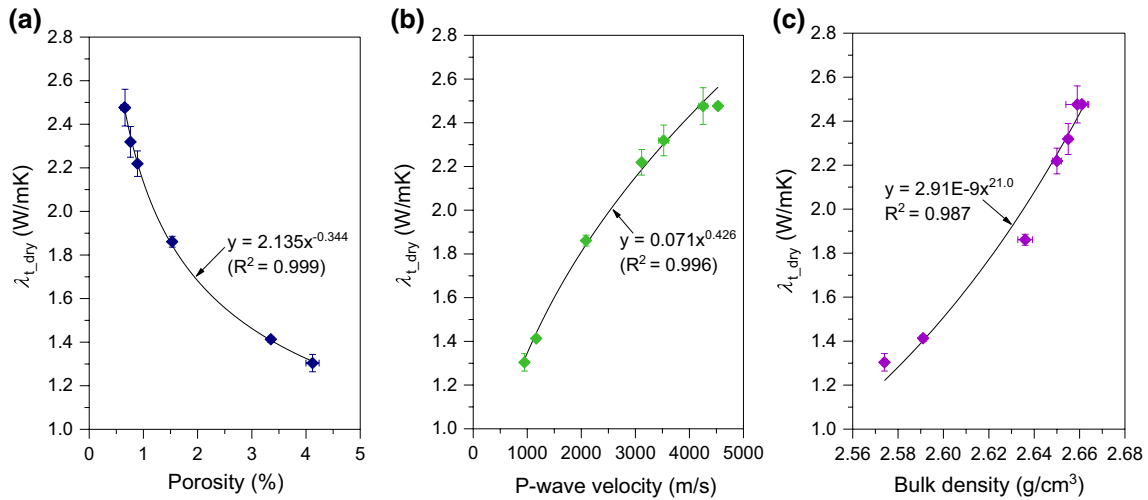


**Fig. 9** Variations of thermal conductivity of the thermally treated specimens with three physical parameters: **a** porosity, **b** P-wave velocity, and **c** bulk density

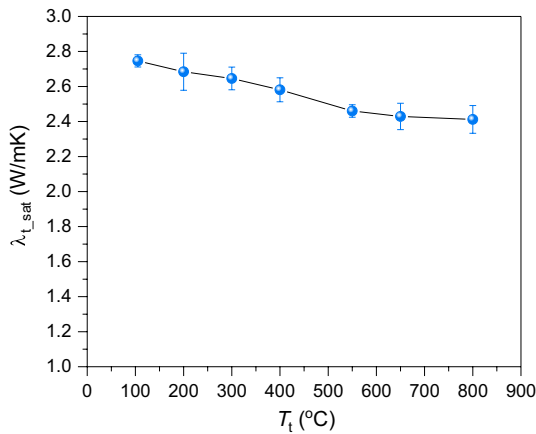


**Fig. 10** Influence of water saturation on thermal conductivity of the specimens treated with different temperatures

occurs when  $T_t$  is higher than 400 °C (see Fig. 5). The primary reason is that water improves the heat transfer capabilities of thermally treated specimens. When thermally damaged specimens were saturated with water, water replaced air in pre-existing and thermally induced microcracks. The water attaches to fractured mineral grain boundaries and damaged mineral grains, increasing the thermal conductivity. For our data set, the average increase in thermal conductivity values of water-saturated thermally treated specimens ranged from 8.4 to 84.9%, versus those under dry conditions. This indicates that water saturation plays an important role in increasing thermal conductivity of thermally damaged specimens.

From thermal conductivity data obtained in both dry and water-saturated conditions for 67 igneous, sedimentary, and

metamorphic rock specimens, Nagaraju and Roy (2014) defined the effect of water saturation on thermal conductivity of rock, which is expressed by

$$S = (\lambda_{\text{sat}} - \lambda_{\text{dry}}) / \lambda_{\text{dry}} \tag{1}$$

where  $\lambda_{\text{sat}}$  and  $\lambda_{\text{dry}}$  are the thermal conductivities of rock in water-saturated and dry states, respectively. Similarly, the effect of water saturation on thermal conductivity of thermally treated rocks can be given by

$$S_t = (\lambda_{t,\text{sat}} - \lambda_{t,\text{dry}}) / \lambda_{t,\text{dry}} \tag{2}$$

Using Eq. (2), the variation of  $S_t$  with  $T_t$  can be obtained, as shown in Fig. 11a. When  $T_t$  is < 400 °C, the influence of water saturation on thermal conductivity of thermally treated specimens is relatively small, and  $S_t$  shows a slowly increasing trend with the increase in  $T_t$ . With further increase in  $T_t$  from 400 to 650 °C,  $S_t$  increases significantly from 16.4 to 71.9%. When  $T_t$  is higher than 650 °C,  $S_t$  continues to increase, but at a slower rate. Previous studies confirmed that the effect of water saturation on thermal conductivity of granitic rocks depended on porosity (Nagaraju and Roy 2014; Zhao et al. 2016). The variation of  $S_t$  with  $T_t$  is in general agreement with porosity evolution against  $T_t$  (Fig. 8a). This means that porosity, which is reflected by thermally induced microcracks, has a significant influence on  $S_t$ .

Based on measurements listed in Table 1, we established the relationship between  $S_t$  and porosity of thermally treated specimens, as shown in Fig. 11b. According to Fig. 11b,  $S_t$  increases with increasing porosity. A linear expression can fit the data reasonably well while ensuring that the line passes through the origin. Based on experimental investigations of thermal conductivity of Beishan granitic rocks with porosities ranging from 0.40 to 1.37%, Zhao et al. (2016)

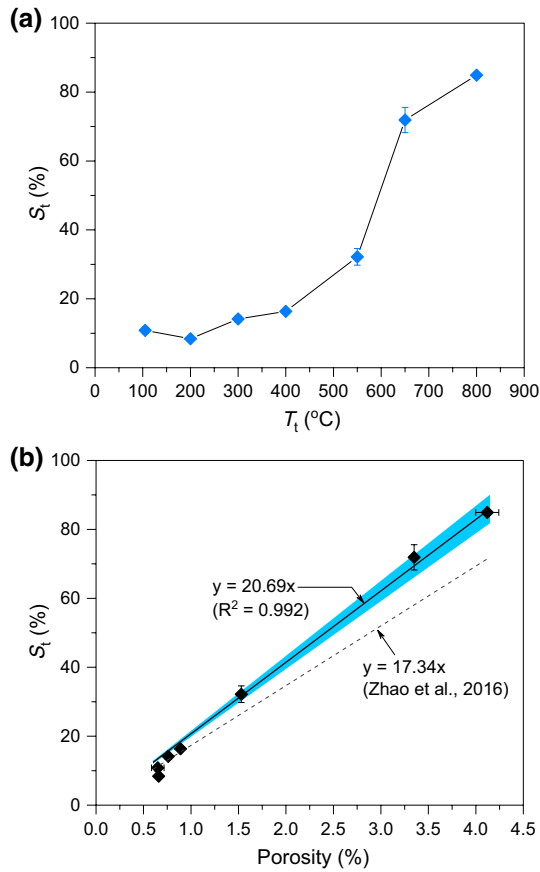


**Fig. 11** **a** Variation of the effect of water saturation ( $S_t$ ) on thermal conductivity of the thermally treated specimens with thermal treatment temperature. **b** Relationship between  $S_t$  and porosity of the thermally treated specimens. The shaded zone in **b** represents the 95% confidence limit for the linear regression

established a linear equation (see Fig. 11b) for the influence of porosity on  $S_t$ . This linear equation accurately captures  $S_t$  of thermally treated specimens with low porosities (<1.0%), but underestimates  $S_t$  of thermally treated specimens with higher porosities (>1.5%). This is not surprising, because thermally treated specimens in this study have a larger porosity range, from 0.65 to 4.12%, which is beyond the boundaries of the previous model (Zhao et al. 2016).

### 4.3 Effect of Ambient Temperature

Figure 12a shows the variation of thermal conductivity of seven pairs of specimens with ambient temperature ( $T$ ) from 40 to 150 °C. The thermal conductivity values (i.e.,  $\lambda_{t,dry}$  values) of these specimens at room temperature (21 °C) were added to this figure. It is seen that for specimens treated with temperatures between 105 and 550 °C, the thermal conductivity gradually decreases with increasing ambient temperature, and the decrease at 150 °C ranges from 3.2 to 7.3% below that at room

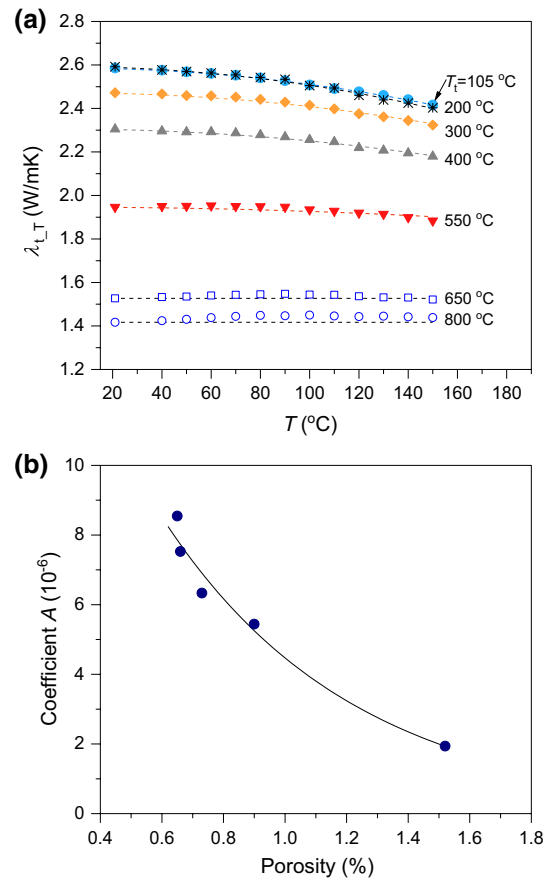


**Fig. 12** **a** Variation of thermal conductivity of seven pairs of the thermally treated specimens with increasing ambient temperature up to 150 °C and their best fits. **b** Variation of fit coefficient  $A$  of the thermal conductivity–temperature curves with porosity of the specimens treated from 105 to 550 °C and its best fit

temperature. This means that within the used ambient temperature range, the influence of increasing temperature on the decay of thermal conductivity for thermally treated rock is small. In addition, for specimens preconditioned at 105 °C and treated at 200 °C, the data are almost the same within the range of ambient temperatures. It is also found that the thermal conductivity decay rate decreases as thermal treatment temperature ( $T_t$ ) increases. For specimens treated at temperatures of 650 and 800 °C, thermal conductivities are not sensitive to  $T$ , and the difference in values for each specimen pair is <0.03 W/mK. Hence, the relation between thermal conductivity and  $T$  can be described using the following piecewise function:

$$\begin{cases} \lambda_{t,T} = \lambda_{t,dry} - AT^2 & 105 \text{ }^\circ\text{C} \leq T_t \leq 550 \text{ }^\circ\text{C} \\ \lambda_{t,T} \approx \lambda_{t,dry} & 650 \text{ }^\circ\text{C} \leq T_t \leq 800 \text{ }^\circ\text{C} \end{cases} \quad (3)$$

where  $\lambda_{t,T}$  is thermal conductivity of thermally treated rock at different ambient temperatures,  $T$  is the ambient temperature (i.e., temperature of oil bath),  $T_t$  is the thermal treatment

**Table 2** Fit coefficient *A* for thermal conductivity–temperature curves of the specimens treated with a temperature ranging from 105 to 550 °C

Specimen pair no.	Thermal treatment temperature (°C)	<i>A</i> (10 <sup>-6</sup> )	<i>R</i> <sup>2</sup>
BS28-1-3	105	7.527	0.998
BS28-2-3	200	8.546	0.992
BS28-3-3	300	6.333	0.981
BS28-4-2	400	5.442	0.979
BS28-5-1	550	1.938	0.737

temperature, and *A* is a fit coefficient (see Table 2). The parameter *A* affects the thermal conductivity decay rate with temperature, i.e., the decay rate increases as *A* increases.

The main minerals in Beishan granite include quartz, plagioclase, K-feldspar, and biotite (see Fig. 2b). Among these, quartz has the highest thermal conductivity (7.69 W/mK), while the others have thermal conductivities ranging between 1.70 and 2.29 W/mK (Horai 1971). Hence, when porosity values are low, quartz content will dictate the thermal conductivity. The thermal conductivity of quartz is sensitive to ambient temperature (Clauser and Huenges 1995), resulting in a gradual decrease in thermal conductivity with increasing temperature. However, when the specimens were treated with high temperatures, the effect of porosity on thermal conductivity strengthens due to the increased number and width of thermally induced microcracks. Thermal conductivity of thermally treated specimens decreases significantly with increasing porosity (see Fig. 9a). Compared with the minerals in granite, the thermal conductivity of air within the microcracks is very low at room temperature (0.026 W/mK; Hilsenrath et al. 1955) and increases with increasing temperature. For example, the thermal conductivity of air is about 0.035 W/mK at 150 °C (Hilsenrath et al. 1955). Hence, with an increase in *T*<sub>i</sub> from 200 to 550 °C, increased microcracks within the specimens restrain the decrease in the thermal conductivity decay rate with increasing *T*, and the decay rate tends to be constant when *T*<sub>i</sub> ranges between 650 and 800 °C (see Fig. 12a). We conclude that parameter *A* in Eq. (3) depends on the porosity (*n*<sub>v</sub>) of the thermally damaged specimens (see Fig. 12b) and varies with porosity according to the following equation:

$$A = 22.37 \exp(-1.61n_v) \tag{4}$$

According to Eqs. (3) and (4), an overall fit for specimens treated with temperatures ranging from 105 to 550 °C is made to illustrate the temperature-dependent thermal conductivity model considering rock porosity. Figure 13 indicates that the results agree well with the results of individual fits based on experimental data. Note that Eqs. (3) and (4) are best-fit curves for thermal conductivity in the range of ambient temperatures. They can

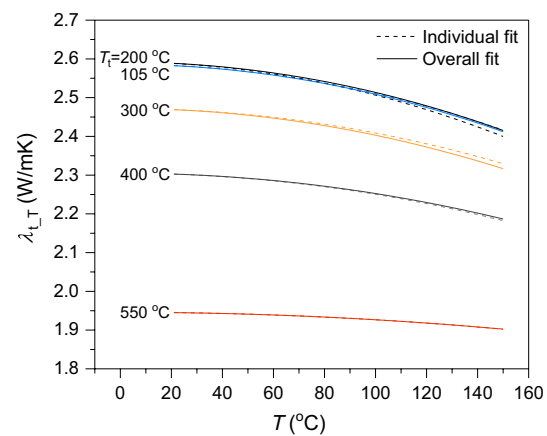


**Fig. 13** Comparison of overall fit using the temperature and rock porosity-dependent thermal conductivity model and individual fit of the specimens treated from 105 to 550 °C

be used to estimate thermal conductivity within this range, but should not be extrapolated to temperatures lower than 21 °C or higher than 150 °C.

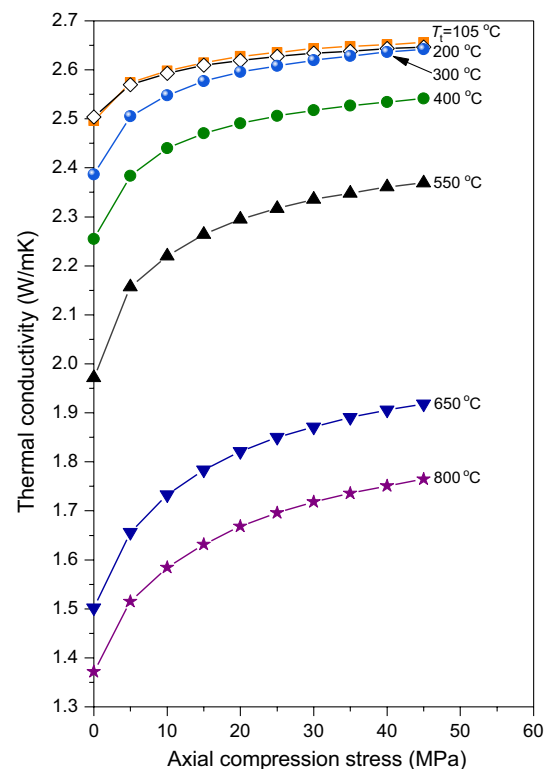


**Fig. 14** Variations of thermal conductivity with axial compression stress of the specimens treated with different temperatures

#### 4.4 Effect of Axial Compression Stress

Thermal conductivity measurements on 14 pairs of specimens were conducted under uniaxial compression, and the results are plotted in Fig. 14. For each rock group, the average thermal conductivity obtained from two pair of specimens was used in our analysis. For each rock group, there is a rapid increase in thermal conductivity at initial loading due to the closure of pores and cracks in the specimens (Fig. 14). The increase rate of thermal conductivity decreases as the load increases, and the thermal conductivity–axial stress relationship shows a convex shape, indicating that the crack closure rate decreases and axial stiffness increases gradually. In subsequent loading, the increase rate of the thermal conductivity changes only slightly, indicating that pores and cracks continue to close slowly under higher compression stress conditions. When the thermally treated specimens are subjected to compression, the effective contact area between mineral grains increases, leading to a large decay of the effect of porosity on thermal conductivity. Meanwhile, the closure of pores and cracks increases the likelihood of contact between quartz grains and thus improves the transportation capability of heat flow in the specimens. In addition, at a given stress level, a higher treatment temperature results in lower thermal conductivity of the rock. For each rock group, the increase rate ( $R_{t,r}$ ) of thermal conductivity can be defined as:

$$R_{t,r} = (\lambda_{t,l} - \lambda_{t,0}) / \lambda_{t,0} \quad (5)$$

where  $\lambda_{t,l}$  and  $\lambda_{t,0}$  are the thermal conductivities of the thermally treated specimens at the highest compression stress (i.e., 45 MPa) and zero stress, respectively. The ratio  $R_{t,r}$  depends on porosity, as shown in Fig. 15.  $R_{t,r}$  increases with increasing porosity and ranges from 5.7 to 28.8%. Analysis

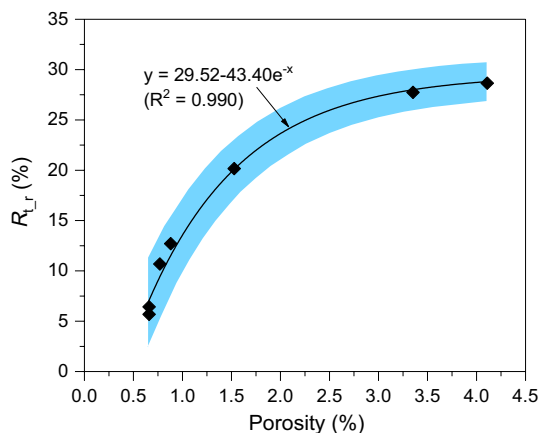


**Fig. 15** Relationship between the increase rate of thermal conductivity ( $R_{t,r}$ ) and porosity for the thermally treated specimens under uniaxial compression. The shaded zone represents the 95% confidence limit for the regression curve

of Figs. 11b and 15 shows that the effects of compression stress and water saturation on thermal conductivity of thermally treated specimens are different. Water saturation has a much greater effect on thermal conductivity of thermally damaged specimens than that of the maximum compression stress used in this study, especially when porosity is  $> 1.5\%$ .

To understand the influence of treatment temperature on thermal conductivity of the specimens under compression, Fig. 16 presents variations in the thermal conductivity ratio ( $R_t$ ) of thermally treated specimens with axial stress.  $R_t$  is defined as

$$R_t = \lambda_{t,c} / \lambda_{t,0} \quad (6)$$

where  $\lambda_{t,c}$  is thermal conductivity of the thermally treated specimens under different compression stresses. For each rock group,  $R_t$  increases nonlinearly with increasing compression stress, and the degree of variation of  $R_t$  depends on the thermal treatment temperature (Fig. 16).

Based on experimental data, a best fitting equation for the axial compression stress-dependent thermal conductivity ratio for the specimens can be expressed as (Demirci et al. 2004; Zhao et al. 2016)

$$R_t = \lambda_{t,c} / \lambda_{t,0} = 1 + B\sigma_1^C \quad (7)$$

where  $\sigma_1$  is the axial compression stress and  $B$  and  $C$  are fit coefficients (see Table 3). As analyzed by Zhao et al. (2016),

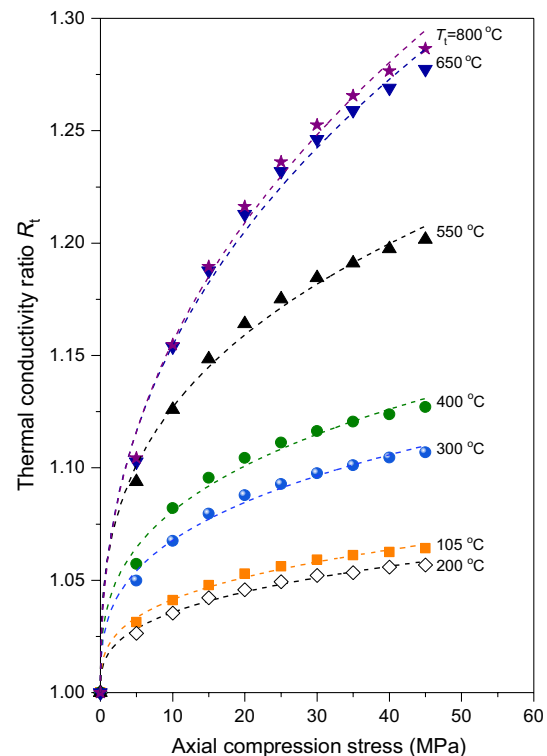


**Fig. 16** Variations of the thermal conductivity ratio with axial compression stress of the specimens treated with different temperatures



**Table 3** Fit coefficients for thermal conductivity ratio–axial compression stress curves of the thermally treated specimens under uniaxial compression

Thermal treatment temperature (°C)	<i>B</i>	<i>C</i>	<i>R</i> <sup>2</sup>
105	0.0203	0.3092	0.984
200	0.0168	0.3274	0.983
300	0.0323	0.3217	0.980
400	0.0385	0.3218	0.969
550	0.0597	0.3274	0.983
650	0.0600	0.4104	0.982
800	0.0589	0.4229	0.986

the coefficient *B* mainly controls the increase gradient of *R<sub>t</sub>* in the initial loading stage. Coefficient *C* plays a critical role in affecting the increase velocity of *R<sub>t</sub>* in the subsequent elastic deformation stage. Coefficient *B* gradually increases from low- to high-temperature treatment conditions until an asymptotic value is reached (Table 3). Coefficient *C* is not sensitive to treatment temperature when the temperature is below 550 °C. With further increase in treatment temperature, *C* presents an increasing trend. Given that thermally induced porosity is closely related to treatment temperature, the relationship between *B* and porosity (see Fig. 17a) can be expressed using an exponential function, as follows:

$$B = 0.06 - 0.37 \exp(-3.31n_t) \tag{8}$$

Coefficient *C* increases slightly with increasing porosity (see Fig. 17b), and a linear equation is used to approximate the trend, as follows:

$$C = 0.294 + 0.032n_t \tag{9}$$

Using Eqs. (7)–(9), an overall fit is made to obtain the rock porosity-dependent thermal conductivity ratio under different axial stresses. A comparison between individual and overall fit results is presented in Fig. 18. The established rock porosity-dependent model can capture the nonlinear compression stress–thermal conductivity ratio relationships of thermally treated Beishan granite satisfactorily. When  $\lambda_{t_0}$  is known, the thermal conductivity of the rock under different compression stresses can be predicted using Eqs. (7)–(9).

Although the above-mentioned results provide insights into the thermal conductivity characteristics of thermally treated Beishan granite subjected to uniaxial compression, one must be aware of the limitation of the used loading condition in representing field rock behavior. In terms of HLW disposal, the current findings only can approximately simulate thermal conductivity of rocks on an unsupported excavation boundary, in which the minimum principal stress ( $\sigma_3$ ) is close to zero. In fact, rocks at depth are under a polyaxial stress state. Hence, knowing the thermal conductivity of

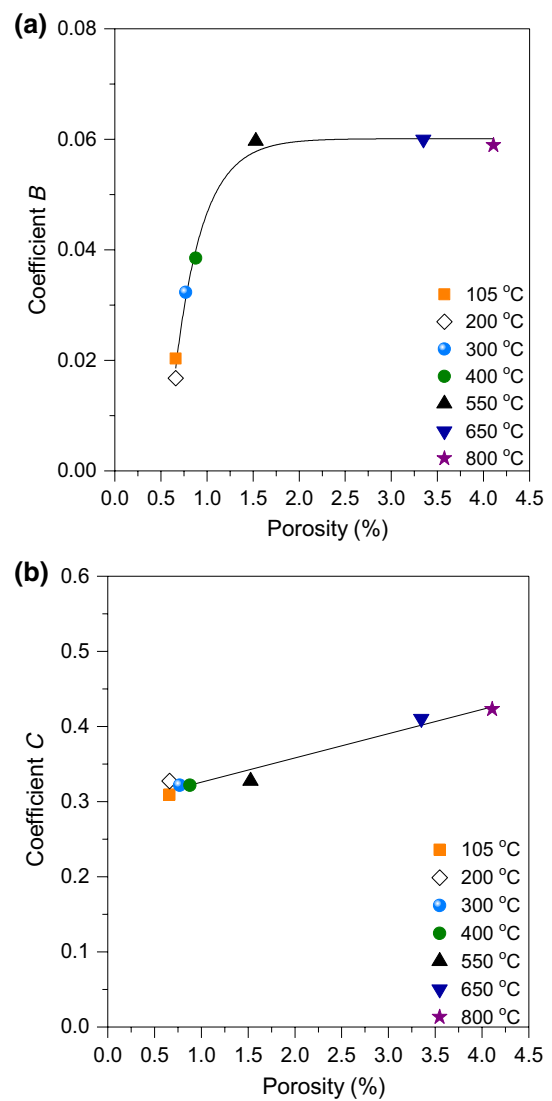


**Fig. 17** Variations of fit coefficients of the thermal conductivity ratio–axial compression stress curves with thermally induced porosity of the specimens treated with different temperatures: **a** coefficient *B* and **b** coefficient *C*

rocks under a triaxial condition would be very important for the design of a HLW repository. However, due to limitations of the experimental facilities, the obtained results do not reveal the influence of different confining stresses on thermal conductivity of specimens during loading. To achieve this goal, further efforts are needed to produce an innovative design for the test equipment.

### 5 Conclusions

Beishan granite is the potential rock for hosting China’s HLW repository. In this study, the effect of thermal treatment on thermal conductivity characteristics of the rock was

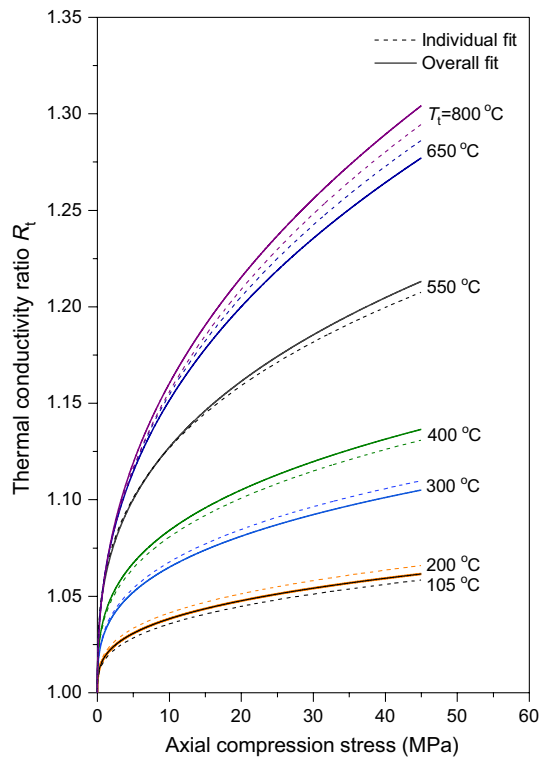


**Fig. 18** Comparison of overall fit using the axial compression stress and porosity-dependent thermal conductivity ratio model and individual fit of the thermally treated specimens

investigated. Basic physical properties such as bulk density, porosity, volume expansion ratio, and P-wave velocity of the thermally treated specimens were also determined. SEM observations were performed to provide evidence for variations in thermal conductivities of the specimens before and after thermal treatment. Furthermore, the influences of water saturation, ambient temperature, and compression stress on thermal conductivity of thermally treated specimens were analyzed. The main findings are as follows:

1. Thermal conductivity of the tested rock depends strongly on the thermal treatment temperature. The thermal conductivity of the thermally treated specimens decreases nonlinearly with increasing temperature from 105 to 800 °C, and the decay rate of thermal conductivity peaks between 550 and 650 °C. As the temperature is increased to 800 °C, the magnitude of thermal conductivity is nearly half that of the specimens before thermal treatment.
2. Variations in bulk density, porosity, volume expansion ratio, and P-wave velocity reveal thermally induced damage characteristics of the specimens from a macroscopic perspective and also reflect thermal conductivity changes with thermal treatment temperature. P-wave velocity and bulk density of the thermally treated speci-

mens are directly proportional to thermal conductivity, while porosity is inversely proportional. In addition, all relationships between thermal conductivity and bulk density, porosity, or P-wave velocity can be described well using power law functions.

3. The deterioration of thermal conductivity of the rock is closely associated with the increase in thermally induced microcracks. When the thermal treatment temperature is increased from 105 to 200 °C, widths of pre-existing microcracks decrease slightly due to thermal expansion of mineral grains. However, the slight microstructural alterations may have a negligible influence on the thermal conductivity. Between 300 and 400 °C, thermally induced inter-granular and intra-granular microcracks are observed. When the treatment temperature is increased up to 650 °C, thermally induced microcracks become more pronounced, and crack density and width increase significantly. When the treatment temperature is 800 °C, inter-granular, intra-granular, and trans-granular microcracks distribute on the specimen surface. The intersection and interconnection of microcracks cause severe damage to the rock, inducing a significant decay of its heat transfer capacity.
4. Water saturation plays an important role in increasing thermal conductivity of thermally treated specimens. As the thermal treatment temperature is increased from 105 to 800 °C, the average increase in thermal conductivity of the water-saturated specimens versus dry conditions ranges from 8.4 to 84.9%. The effect of water saturation on thermal conductivity of thermally treated specimens increases approximately linearly with increasing rock porosity.
5. Thermal conductivity characteristics of thermally treated specimens are temperature and compression stress dependent. Within the ambient temperature range from room temperature to 150 °C, the influence of temperature on thermal conductivity of the thermally treated specimens is small. Meanwhile, thermally induced microcracks can restrain the decrease in the thermal conductivity decay rate with increasing temperature. A temperature-dependent thermal conductivity model considering rock porosity was proposed for specimens treated with temperatures ranging from 105 to 550 °C. In addition, thermal conductivity of the thermally treated specimens increases with increasing compression stress from 0 MPa to 45 MPa, and at a given compression stress, a higher treatment temperature results in lower thermal conductivity. Moreover, the increase rate of thermal conductivity increases nonlinearly with increasing porosity. Based on experimental data, an empirical model was established for predicting thermal conductivity characteristics of thermally treated specimens under compression, and the predictions were found to

be in good agreement with experimental results. Further efforts are needed to reveal the influence of different confining stresses on thermal conductivity behaviors of thermally treated Beishan granite during triaxial compression.

**Acknowledgements** This work has been supported by the China Atomic Energy Authority through the geological disposal program.

## References

- Adl-Zarrabi B (2004) Thermal properties: heat conductivity and heat capacity determined using the TPS method and mineralogical composition by modal analysis. Svensk Kärnbränslehantering AB, Oskarshamn
- Ahn J, Apted MJ (2010) Geological repository systems for safe disposal of spent nuclear fuels and radioactive waste. Woodhead Publishing Limited, Cambridge
- Birch F, Clark H (1940) The thermal conductivity of rocks and its dependence upon temperature and composition. *Am J Sci* 238:613–635
- Chaki S, Takarli M, Agbodjan WP (2008) Influence of thermal damage on physical properties of a granite rock: porosity, permeability and ultrasonic wave evolutions. *Constr Build Mater* 22:1456–1461
- Chen S, Yang C, Wang G (2017) Evolution of thermal damage and permeability of Beishan granite. *Appl Therm Eng* 110:1533–1542
- Cho WJ, Kwon S (2010) Estimation of the thermal properties for partially saturated granite. *Eng Geol* 115:132–138
- Cho WJ, Kwon S, Choi JW (2009) The thermal conductivity for granite with various water contents. *Eng Geol* 107:167–171
- Clauser C, Huenges E (1995) Thermal conductivity of rocks and minerals. In: Ahrens TJ (ed) *Rock physics and phase relations: a handbook of physical constants*. American Geophysical Union, Washington, pp 105–126
- David C, Menéndez B, Darot M (1999) Influence of stress-induced and thermal cracking on physical properties and microstructure of La Peyratte granite. *Int J Rock Mech Min Sci* 36:433–448
- Demirci A, Görgülü K, Durutürk YS (2004) Thermal conductivity of rocks and its variation with uniaxial and triaxial stress. *Int J Rock Mech Min Sci* 41:1133–1138
- Fredrich JT, Wong TF (1986) Micromechanics of thermally induced cracking in three crustal rocks. *J Geophys Res* 91:12743–12764
- Freire-Lista DM, Fort R, Varas-Muriel MJ (2016) Thermal stress-induced microcracking in building granite. *Eng Geol* 206:83–93
- Géraud Y (1994) Variations of connected porosity and inferred permeability in a thermally cracked granite. *Geophys Res Lett* 21:979–982
- Gustafsson SE (1991) Transient plane source techniques for thermal conductivity and thermal diffusivity measurements of solid materials. *Rev Sci Instrum* 62:797–804
- Hartmann A, Rath V, Clauser C (2005) Thermal conductivity from core and well log data. *Int J Rock Mech Min Sci* 42:1042–1055
- Heard HC, Page L (1982) Elastic moduli, thermal expansion, and inferred permeability of two granites to 350 °C and 55 megapascals. *J Geophys Res* 87:9340–9348
- Heuze FE (1983) High-temperature mechanical, physical and thermal properties of granitic rocks—a review. *Int J Rock Mech Min Sci Geomech Abstr* 20:3–10
- Hilsenrath J, Beckett CW, Benedict WS, Fano L, Hoge HJ, Masi JF, Nuttall RL, Touloukian YS, Woolley HW (1955) Tables of thermal properties of gases. United States Government Printing Office, Washington
- Homand-Etienne F, Houpert R (1989) Thermally induced microcracking in granites: characterization and analysis. *Int J Rock Mech Min Sci Geomech Abstr* 26:125–134
- Homand-Etienne F, Troalen J-P (1984) Behaviour of granites and limestones subjected to slow and homogeneous temperature changes. *Eng Geol* 20:219–233
- Horai K (1971) Thermal conductivity of rock-forming minerals. *J Geophys Res* 76:1278–1308
- Hot Disk (2007) Instruction manual of Hot Disk thermal constants analyser. Hot Disk AB, Gothenburg
- Hudson JA, Cosgrove JW, Kemppainen K, Johansson E (2011) Faults in crystalline rock and the estimation of their mechanical properties at the Olkiluoto site, western Finland. *Eng Geol* 117:246–258
- Inserra C, Biwa S, Chen Y (2013) Influence of thermal damage on linear and nonlinear acoustic properties of granite. *Int J Rock Mech Min Sci* 62:96–104
- ISRM (1979) Suggested methods for determining water content, porosity, density, absorption and related properties and swelling and slake-durability index properties. *Int J Rock Mech Min Sci Geomech Abstr* 16:143–151
- Jansen DP, Carlson SR, Young RP, Hutchins DA (1993) Ultrasonic imaging and acoustic emission monitoring of thermally induced microcracks in Lac du Bonnet granite. *J Geophys Res* 98:22231–22243
- Kumari WGP, Ranjith PG, Perera MSA, Shao S, Chen BK, Lashin A, Arifi NA, Rathnaweera TD (2017) Mechanical behaviour of Australian Strathbogie granite under in situ stress and temperature conditions: an application to geothermal energy extraction. *Geothermics* 65:44–59
- Kumari WGP, Ranjith PG, Perera MSA, Chen BK (2018) Experimental investigation of quenching effect on mechanical, microstructural and flow characteristics of reservoir rocks: thermal stimulation method for geothermal energy extraction. *J Petrol Sci Eng* 162:419–433
- Lagüela S, Bison P, Peron F, Romagnoni P (2015) Thermal conductivity measurements on wood materials with transient plane source technique. *Thermochim Acta* 600:45–51
- Lima JJDC, Paraguassú AB (2004) Linear thermal expansion of granitic rocks: influence of apparent porosity, grain size and quartz content. *Bull Eng Geol Env* 63:215–220
- Liu S, Xu J (2014) Mechanical properties of Qinling biotite granite after high temperature treatment. *Int J Rock Mech Min Sci* 71:188–193
- Log T, Gustafsson SE (1995) Transient plane source (TPS) technique for measuring thermal transport properties of building materials. *Fire Mater* 19:43–49
- Mahmutoglu Y (1998) Mechanical behaviour of cyclically heated fine grained rock. *Rock Mech Rock Eng* 31:169–179
- Menéndez B, David C, Darot M (1999) A study of the crack network in thermally and mechanically cracked granite samples using confocal scanning laser microscopy. *Phys Chem Earth Part A* 24:627–632
- Menéndez B, David C, Nistal AM (2001) Confocal scanning laser microscopy applied to the study of pore and crack networks in rocks. *Comput Geosci* 27:1101–1109
- Miao SQ, Li HP, Chen G (2014) Temperature dependence of thermal diffusivity, specific heat capacity, and thermal conductivity for several types of rocks. *J Therm Anal Calorim* 115:1057–1063
- Michel D, Yves G, Marie-Laure B (1992) Permeability of thermally cracked granite. *Geophys Res Lett* 19:869–872
- Nagaraju P, Roy S (2014) Effect of water saturation on rock thermal conductivity measurements. *Tectonophysics* 626:137–143
- Nasseri MHB, Schubnel A, Young RP (2007) Coupled evolutions of fracture toughness and elastic wave velocities at high crack

- density in thermally treated Westerly granite. *Int J Rock Mech Min Sci* 44:601–616
- Özkahraman HT, Selver R, Işık EC (2004) Determination of the thermal conductivity of rock from P-wave velocity. *Int J Rock Mech Min Sci* 41:703–708
- Pasquale V, Verdoya M, Chiozzi P (2015) Measurements of rock thermal conductivity with a Transient Divided Bar. *Geothermics* 53:183–189
- Peng J, Rong G, Cai M, Yao MD, Zhou CB (2016) Physical and mechanical behaviors of a thermal-damaged coarse marble under uniaxial compression. *Eng Geol* 200:88–93
- Ramires MLV, Nieto de Castro CA, Nagasaka Y, Nagashima A, Assael MJ, Wakeham WA (1995) Standard reference data for the thermal conductivity of water. *J Phys Chem Ref Data* 24:1377–1381
- Ray L, Bhattacharya A, Roy S (2007) Thermal conductivity of Higher Himalayan Crystallines from Garhwal Himalaya, India. *Tectonophysics* 434:71–79
- Richter D, Simmons G (1974) Thermal expansion behavior of igneous rocks. *Int J Rock Mech Min Sci Geomech Abstr* 11:403–411
- Shao S, Ranjith PG, Wasantha PLP, Chen BK (2015) Experimental and numerical studies on the mechanical behaviour of Australian Strathbogie granite at high temperatures: an application to geothermal energy. *Geothermics* 54:96–108
- Simmons G, Cooper HW (1978) Thermal cycling cracks in three igneous rocks. *Int J Rock Mech Min Sci Geomech Abstr* 15:145–148
- Solórzano E, Reglero JA, Rodríguez-Pérez MA, Lehmann D, Wichmann M, de Saja JA (2008) An experimental study on the thermal conductivity of aluminium foams by using the transient plane source method. *Int J Heat Mass Transf* 51:6259–6267
- Sun Q, Zhang W, Xue L, Zhang Z, Su T (2015) Thermal damage pattern and thresholds of granite. *Environ Earth Sci* 74:2341–2349
- Sundberg J, Back PE, Ericsson LO, Wrafter J (2009a) Estimation of thermal conductivity and its spatial variability in igneous rocks from in situ density logging. *Int J Rock Mech Min Sci* 46:1023–1028
- Sundberg J, Back PE, Christiansson R, Hökmark H, Ländell M, Wrafter J (2009b) Modelling of thermal rock mass properties at the potential sites of a Swedish nuclear waste repository. *Int J Rock Mech Min Sci* 46:1042–1054
- Urquhart A, Bauer S (2015) Experimental determination of single-crystal halite thermal conductivity, diffusivity and specific heat from  $-75\text{ }^{\circ}\text{C}$  to  $300\text{ }^{\circ}\text{C}$ . *Int J Rock Mech Min Sci* 78:350–352
- Wang J (2010) High-level radioactive waste disposal in China: update 2010. *J Rock Mech Geotech Eng* 2:1–11
- Wang J (2014) On area-specific underground research laboratory for geological disposal of high-level radioactive waste in China. *J Rock Mech Geotech Eng* 6:99–104
- Wang HF, Bonner BP, Carlson SR, Kowallis BJ, Heard HC (1989) Thermal stress cracking in granite. *J Geophys Res* 94:1745–1758
- Xu G, LaManna JM, Clement JT, Mench MM (2014) Direct measurement of through-plane thermal conductivity of partially saturated fuel cell diffusion media. *J Power Sources* 256:212–219
- Yang Y, Voskuilen TG, Pourpoint TL, Guildenbecher DR, Gore JP (2012) Determination of the thermal transport properties of ammonia borane and its thermolysis product (polyiminoborane) using the transient plane source technique. *Int J Hydrogen Energy* 37:5128–5136
- Yang SQ, Ranjith PG, Jing HW, Tian WL, Ju Y (2017) An experimental investigation on thermal damage and failure mechanical behavior of granite after exposure to different high temperature treatments. *Geothermics* 65:180–197
- Yavuz H, Demirdag S, Caran S (2010) Thermal effect on the physical properties of carbonate rocks. *Int J Rock Mech Min Sci* 47:94–103
- Yong C, Wang C (1980) Thermally induced acoustic emission in westerly granite. *Geophys Res Lett* 7:1089–1092
- Zhang W, Sun Q, Hao S, Geng J, Lv C (2016) Experimental study on the variation of physical and mechanical properties of rock after high temperature treatment. *Appl Therm Eng* 98:1297–1304
- Zhang F, Zhao JJ, Hu DW, Skoczylas F, Shao JF (2018) Laboratory investigation on physical and mechanical properties of granite after heating and water-cooling treatment. *Rock Mech Rock Eng* 5:677–694
- Zhao Z (2016) Thermal influence on mechanical properties of granite: a microcracking perspective. *Rock Mech Rock Eng* 49:747–762
- Zhao XG, Wang J, Chen F, Li PF, Ma LK, Xie JL, Liu YM (2016) Experimental investigations on the thermal conductivity characteristics of Beishan granitic rocks for China's HLW disposal. *Tectonophysics* 683:124–137
- Zhao Z, Liu Z, Pu H, Li X (2018) Effect of thermal treatment on Brazilian tensile strength of granites with different grain size distributions. *Rock Mech Rock Eng* 51:1293–1303